ELSEVIER

Physica D 96 (1996) 132–161

PHYSICA D

Analyzing the dynamics of cellular flames

Antonio Palacios [a], Dieter Armbruster [a,*], Eric J. Kostelich [a], Emily Stone [b]

[a] *Department of Mathematics, Arizona State University, Tempe, AZ 85287-1804, USA*

[b] *Department of Mathematics and Statistics, Utah State University, Logan, UT 84322-3900, USA*

Abstract

Video data from experiments on the dynamics of two-dimensional flames are analyzed. The Karhunen–Loéve (KL) analysis is used to identify the dominant spatial structures and their temporal evolution for several dynamical regimes of the flames. A data analysis procedure to extract and process the boundaries of flame cells is described. It is shown how certain spatial structures are associated with certain temporal events. The existence of small scale, high frequency, turbulent background motion in almost all regimes is revealed.

1. Inroduction

The Karhunen–Loéve analysis (or proper orthogonal decompostition) has recently generated a lot of interest in its ability to analyze and model complex spatio-temporal data [5]. Most applications have concentrated on modeling PDE simulations with optimal eigenfunctions, thus generating a smaller Galerkin system that behaves like the large scale simulation of the PDE ([3], see also the references in [5]). We want to report here on an ongoing project to extract phase space information out of experimental data for which there is no generally agreed upon model. As a result there is no straightforward way of reducing these data via a Galerkin projection to the evolution of a few ODEs. By "phase space information" we mean the identification of periodic, quasiperiodic and chaotic behavior and their generating spatial structures. We also seek to identify unstable steady states or unstable periodic orbits and their stable and unstable manifolds that generate bursting behavior through heteroclinic cycles. In addition, we hope to determine linear spanning dimensions for any kind of chaotic behavior and we expect to be able to identify the bifurcations that have occurred when one observes a change in the experiment upon changes in a parameter.

We consider data from an experiment on the dynamics of two-dimensional flames [7]. The experiment consists of a flat circular porous burner which burns premixed gases. The shape of the flames, when viewed from the top, changes when the gas mixtures and the feeding pressures are altered. A video camera records the resulting flame dynamics. Typically one sees an unsteady motion of one or more flame cells which show up as bright circles on a dark background. Common regimes show two concentric rings of flame cells that move: they rotate with and against each other, some of the cells merge and split and show intermittent behavior with a long stationary configuration of cells that eventually changes quickly to another quasi-stationary configuration. From visual observations and from other tests that have been performed [6],

* Corresponding author.

PII S0167-2789(96)00017-6

one expects a KL analysis to yield useful information about the type and origin of the unsteady flame dynamics. We note also that there is considerable debate as to the correct PDE model for this experiment. There are oversimplified reaction diffusion type models for one-dimensional flames [4] but little agreement on simplistic two-dimensional models. Better models are extremely complicated because they involve chemistry, hydrodynamics, and thermodynamics. There is also considerable speculation on the nature of the flame dynamics: Quasiperiodic, chaotic, heteroclinic and metastable are some of the attributes that have been used [6–8]. Therefore, we believe that a description of these experiments in terms of structures in phase space would be extremely valuable.

Since the Karhunen–Loéve analysis has been described in great detail in many recent publications [5,15] we will describe here the main idea only.

Consider a data set $u(x,t)$ defined over a finite spatial domain R and given for a finite interval $0 \le t \le T$. Assume that the average $\langle u(x,t)\rangle$, which is usually a time average, is zero. The KL analysis finds a set of orthogonal functions $\psi(x)$ which, on the average, are optimally aligned with the data set. These functions $\psi(x)$ are the eigenfunctions of a correlation matrix and are called the empirical eigenfunctions [11], coherent structures [15], etc. It can be shown that any projection of the data $u(x,t)$ onto a finite set of the ψ_j, given by

$$u_N = P_N u = \sum_{k=1}^{N} a_k(t)\psi^{(k)}(x)$$

leads to uncorrelated (with respect to the averaging process) amplitudes a_k such that $\langle a_j(t)a_k(t)\rangle = \lambda_j \delta_{jk}$, where λ_j is the variance of the data in the direction of the jth eigenfunction. The error, which is given by $\varepsilon_N = ||u - u_N||^2$, is a minimum over all possible sets of orthonormal functions for any given N. The *energy* of the data is defined as the sum of the eigenvalues of the correlation function: $E = \sum_{i=1} \lambda_i$. We can reconstruct any sample vector using the eigenfunctions

$$u(x,t_0) = \sum_{k=1}^{N} a_k(t_0)\psi^{(k)}(x), \tag{1}$$

where the coefficients are computed from the projection of the sample vector onto an eigenfunction

$$a_k(t_0) = (u(x,t_0), \psi^{(k)}(x)). \tag{2}$$

An approximation to the data can be constructed with the first K most energetic eigenfuctions by

$$u(x,t) \approx \sum_{i=1}^{K} a_i \psi^{(i)}. \tag{3}$$

We are using a software package, called KLTOOL, to analyze spatio-temporal data using the Karhunen–Loéve (KL) decomposition. KLTOOL was written by Randy Heiland [1] as a user-friendly, flexible program that automates many of the steps in a KL analysis and permits graphical representation of the results.

A large part of this paper is the description of a reduction of the video images of the flames into a format that KLTOOL can handle efficiently. To begin with, we restrict our attention to the motion of the borders of the cells, since in the regimes we are studying there is very little apparent structure inside the cells; they appear to be uniformly white. This obviously ignores some parts of the dynamics and should be viewed as a first order approximation to the full flame dynamics, but one that yields much information none the less. Thus we require the translation of the two-dimensional image into information about the cells' outlines only. We devote a section to describing this process, which we believe is a novel combination of known techniques adapted for use on these data sets.

Section 2 contains a brief description of specific regimes of the flame experiment studied (denoted rotating, ratcheting and pinwheel). The results of a preliminary study [13] on the KL analysis of cell border data is summarized in Section 3. Section 4 details the techniques used in extracting the outlines, mentioned above. Finally in Section 5, we present the results of the KL analysis applied to the data set reductions from the three flame regimes.

In summary, the purpose of this work is to develop an *efficient* and *reliable* measure that can quantify, from a sequence of video images, the motion of cellular flames as they change with time. The procedure must be tractable from the computational point of view

and make the best use of the existing laboratory data. Highly resolved spatio-temporal data sets are needed in order to capture some features of the dynamics. Ideally, we would like to have large two-dimensional time series with high spatial resolution encapsulating all aspects of the dynamics. Realistically, this is impossible with current computer technology. However, we succeed for several flame regimes in separating large scale periodic and quasiperiodic motion from a turbulent background. We identify the spatial structures responsible for certain temporal events. We present evidence that the highly irregular background motion of the cells is better described in analogy to hydrodynamic turbulence (i.e. a large number of degrees of freedom) than as low-dimensional chaos.

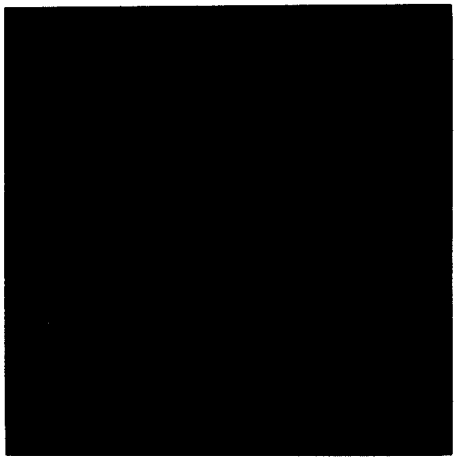

Fig. 1. A snapshot of the rotating regime.

2. Experimental observations

As different dynamic regimes in isobutane-air flames compete for stability, different types of rotating cellular flames become visible. In this section we describe the dynamics of three regimes: a rotating ring of outer cells around a seemingly stable inner ring, a ring of cells rotating fast around a center cell that itself changes its shape, and two rings of cells that each rotate and whose motion is interrelated in a complicated way. We call the three cases the rotating, the pinwheel and the ratcheting regime, respectively.

2.1. Rotating regime

The physical simplicity of a rigid rotating state makes it a good place to start a quantitative description of the flame dynamics. We have captured a sequence of 249 video frames from a regular $\frac{1}{2}''$ VHS tape of a rotating state consisting of an outer ring of twelve cells concentric with an inner ring of five cells. The original images suggest a regime where the overall dynamics are dominated by a clockwise rigid rotation of the outer ring when the inner ring stays fixed. However, a careful observation reveals the presence of more complicated dynamics. The outer ring rotates clockwise with two alternating speeds: it moves slowly for a long period of time and then significantly faster for a short time. This cycle repeats periodically during the 360° rotation performed by the outer ring. The inner ring starts the sequence (first 10 frames) with a small clockwise rotation of approximately ten degrees. It then remains stationary throughout most of the remaining sequence. During this time, a significant amount of activity on the inner ring, both in shape changes and in small scale motion of individual cells, is observed. Then, towards the end of the animation (around frame 200) the inner ring executes a 90° clockwise rotation away from its previous position. It then remains on this new position until the end of the video sequence. Fig. 1 shows one typical video frame for this scenario. The video image has a resolution of 320 × 240 pixel. There is noise surrounding the cells that is introduced during the recording process, but the outlines of the cells are still well defined.

2.2. Pinwheel regime

A second interesting regime where rotating cellular flames are observed is illustrated in Fig. 2. It consists of a single ring of six cells surrounding one central cell. In this case, the ring rotates counterclockwise at a very fast speed of approximately $270°s^{-1}$, giving the appearance of a fast spinning wheel. The direction of rotation depends on the initial conditions of the experiment. A similar regime with a clockwise rotation is also observed. The ordered pattern is not steady.

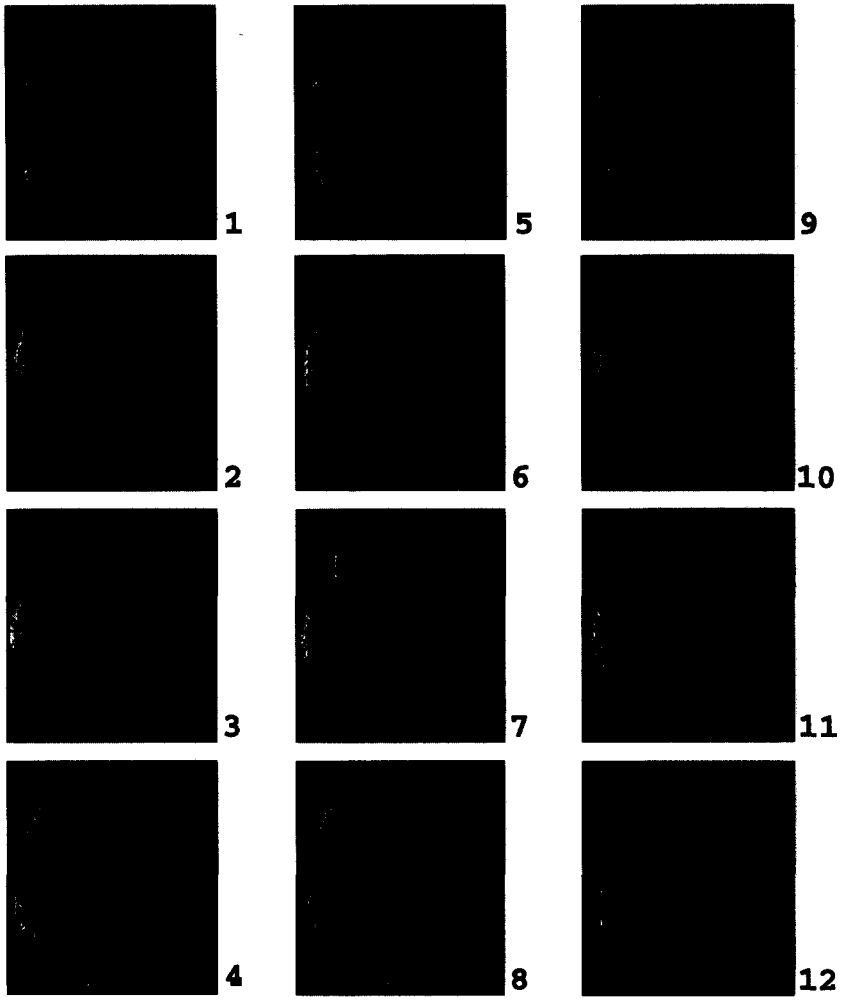

Fig. 2. A fast rigid rotation in a single ring of cellular flames surrounding a central cell.

The cells subtly change their size and shape, and they exhibit significant amplitude oscillations about their equilibrium position as the entire ring continues to rotate. Gorman et al. [6] speculate that "chaotic motion of the outer ring" perturbs the inner cell, causing it to change size.

A video sequence of 140 frames was captured from the tape, at a rate of 30 frames s^{-1} (compared to 15 frames s^{-1} used in the rotating regime). In this way, the motion of the cells appears as continuous as possible, the ordering of the cells is clear, and a more accurate description of the dynamics is obtained. Fig. 2 shows an edited sequence of 12 consecutive frames. A black dot labels one cell and tracks the rotating motion. Computer memory limitations have forced us to reduce the resolution of each image to 120×90 pixel (a trade-off between spatial and temporal resolution).

2.3. Ratcheting regime

This regime exhibits a ratcheting dynamics of two concentric rings of thirteen and six cells surrounding one central cell. Both rings slowly rotate at a rate of approximately $1°s^{-1}$, when locked through an angle of approximately 16°. The inner ring then unlocks and snaps back to its original position. The rapid

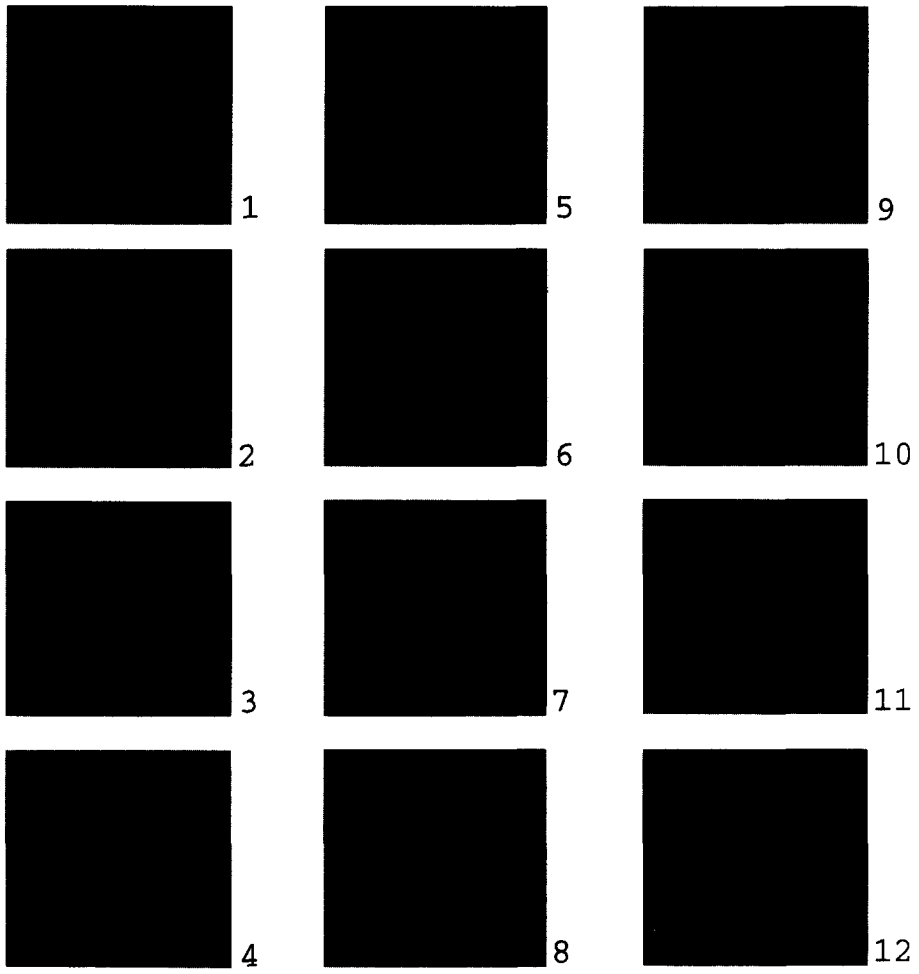

Fig. 3. A ratcheting cycle simulated by twelve sequential video images. A dot traces an individual cell motion in each ring. Both rings rotate clockwise while locked in frames 1–5. In frame 6, the inner ring unlocks and rotates back to its original position in frame 12.

snap-back of the inner ring is followed by a significant deceleration of the outer ring. The process repeats itself periodically as the outer ring continues to rotate clockwise. The ratcheting motion can be thought of in a mechanical way: the two rings behave as if they were rigid toothed gears. A ratcheting cycle is illustrated by the twelve snapshots of Fig. 3 in which only the upper right quadrant of each image is shown to aid the visualization of the ratcheting motion. A dot marks the trace of an individual cell in each ring. The figure shows the relative angular rotation of the two rings. At the beginning of the sequence both rings are locked and continue to rotate clockwise throughtout the first six frames. In frame 6, the inner ring unlocks and starts rotating counterclockwise until it returns to its original position in frame 12. In a recorded sequence of 406 video images, the ratcheting cycle repeats itself periodically, about 18 times, and the outer ring executes a rotation of approximately 500°. Each image has a constant resolution of 320 × 240 pixel.

Gorman et al. [8] note that ratcheting (time dependent) and ordered (stationary) states co-exist in parameter space: the asymptotic behavior of the system depends on the inital conditions. They assert that this

regime is best described as independent, interacting concentric rings of cells rather than individual cells interacting with their nearest neighbors.

3. Cell boundary data analysis

In order to apply the KL decomposition to the flame data it is necessary to digitize and represent the frames in the video as sample data vectors. As mentioned in Section 1, we are interested in analyzing the dynamics of the cell boundaries. In [13] the boundary curve for a single cell is represented as a 1-d vector in polar coordinates: $r(\theta_i)$ for a fixed angular resolution $1 \leq i \leq N$. This representation is well suited for the single cell regime but is more difficult to apply to regimes with multiple cells. For such regimes with a fixed number of cells, we have devised an extension of the polar coordinate method. To perform KL on the cells we take a piecewise linear approximation to the boundary of each cell. Each cell is represented by the vertices of an n-gon. Details of the algorithm are given in Section 4. Each vertex of the n-gon has coordinates (x_i, y_i), and hence the whole cell is represented by an n-dimensional 2-vector. One snapshot of N-cell outlines then becomes an $(n \times N)$-dimensional 2-vector, A. The ensemble of M snapshots is $\{\mathbf{A}^k\}, k = 1, \ldots, M$.

Applying KL means finding an optimal basis for the ensemble

$$\mathbf{A}^k = \sum_{j=1} a_j^k \psi^j,$$

where we choose to view $\mathbf{A}^k$ as an $n \cdot N$-dimensional complex vector, so that both a_j^k and ψ^j are now complex. In the following results, KLTOOL was used to do all eigenfunction calculations.

In an earlier paper [13] we describe work done on "mock data" made up of outlines of multiple cells, to test this data set representation. For more details see [13]. We reproduce the simplest results here, in order to introduce the reader to the interpretation of the results of KL applied to the multiple cell boundary vectors.

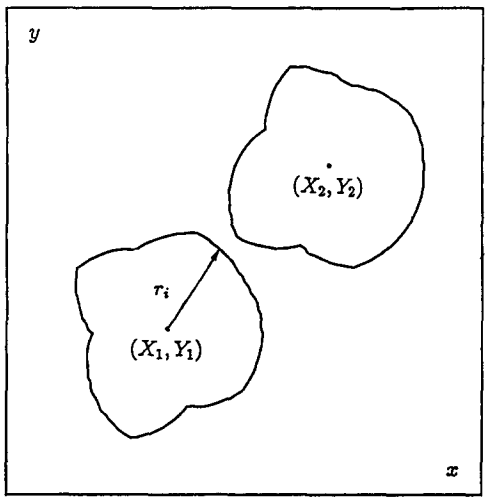

Fig. 4. Two sample constructed cells.

Two cell outlines are constructed for each snapshot by distorting two circles of the same radius, R, placed with their centers at (X_1, Y_1) and (X_2, Y_2). A sample of this data is shown in Fig. 4. Each cell is represented by a regular n-gon. The distance of the ith vertex from the center of the n-gon is given by $r_i = R + \varepsilon\xi_i$, where ε is a scale parameter and ξ_i is determined by successive iterations of the logistic map:

$$\xi_{i+1} = \Gamma\xi_i(1 - \xi_i),$$

where Γ is a tuning parameter. In this way, the complexity in the variation on the boundary can be tuned, since as Γ varies from 2.0 to 4.0, the logistic map undergoes a sequence of period-doubling bifurcations. A periodic variation of the boundary can be achieved by setting Γ to values at which the logistic map has a periodic orbit. In the cases that follow, we choose $\Gamma = 3.8$, where the behavior of the logistic map possesses the same statistics as a random walk (at this parameter value we are essentially using the map as a random number generator). For the purpose of drawing the cells, points on the boundary in between the n endpoints are calculated by linearly interpolating the radius between $R + \varepsilon\xi_{i+1}$ and $R + \varepsilon\xi_i$. Values of ε and Γ are chosen to best approximate the appearance of the experimental cells. In order to mimic the fine scale fuzziness of the experimental data, a random

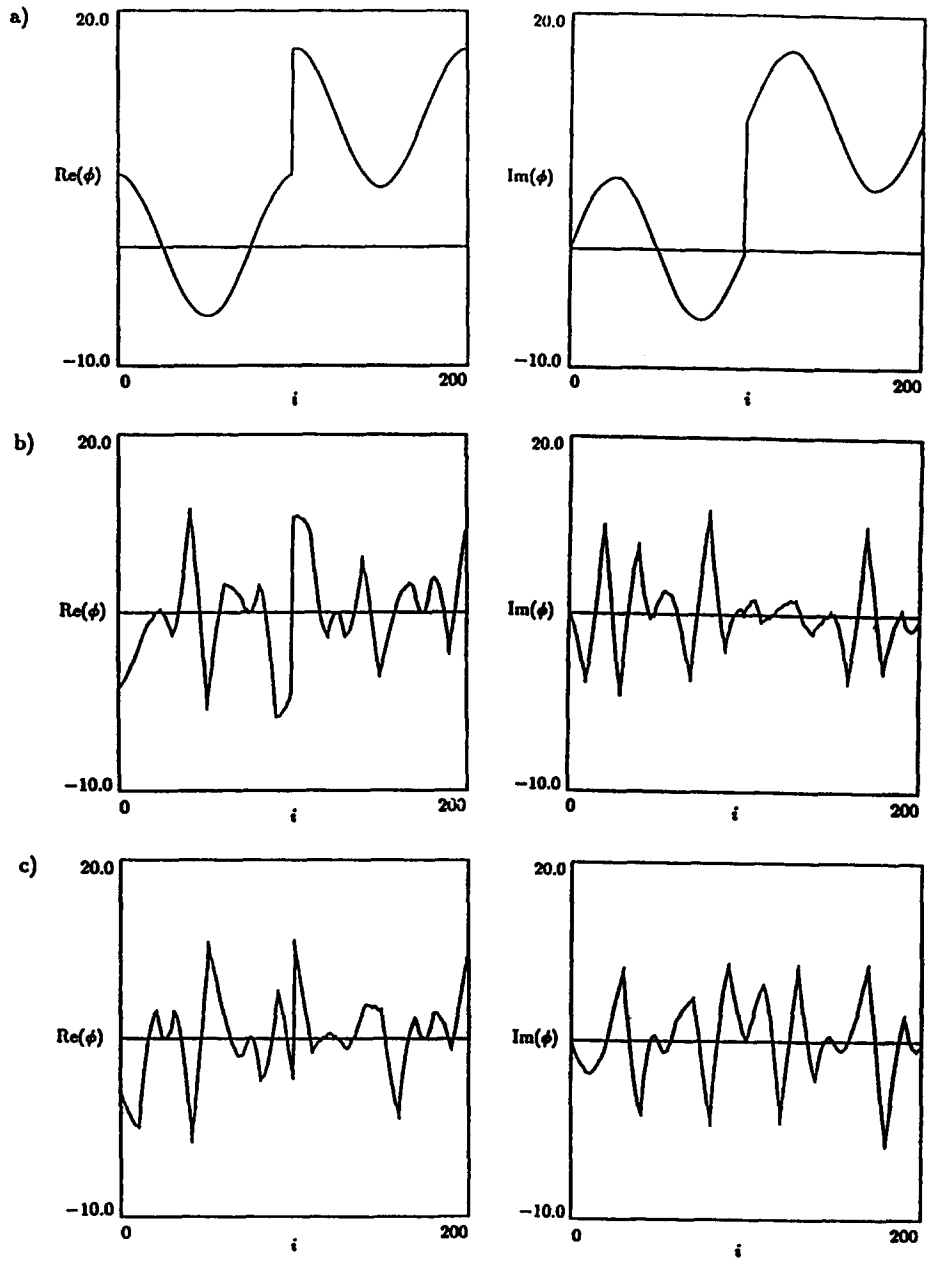

Fig. 5. (a) Zeroth eigenfunction (mean), real and imaginary parts, (b) first eigenfunction, (c) second eigenfunction.

noise of small amplitude is added to the distorted radius at each point.

Each snapshot consists of 200 complex numbers representing two cells. The first 100 complex numbers represent one cell, the next 100 numbers represent the other. The KL spectrum calculated from two cells with fixed center points (meaning that (X_1, Y_1) and (X_2, Y_2) did not vary from snapshot to snapshot) with $\Gamma = 3.8$ shows that 98% of the variance is captured with the first 14 eigenfunctions, a compression ratio of approximately 1 to 4. The ensemble was comprised of 50 snapshots, so 50 eigenfunctions can be

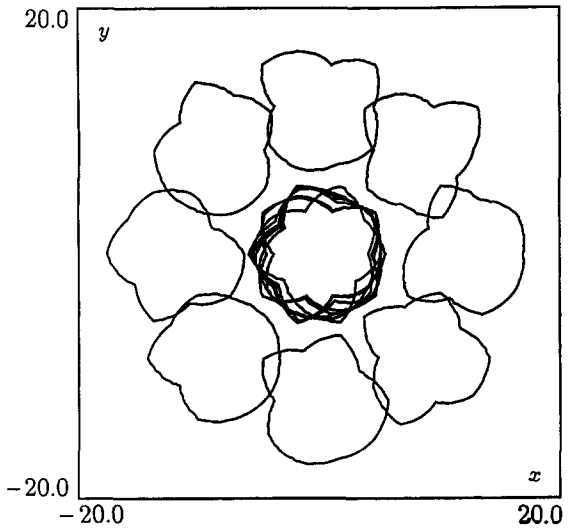

Fig. 6. Sample synthetic rotating data, eight overlaid snapshots.

constructed. The first three eigenfunctions, real and imaginary parts, are plotted in Fig. 5. The zeroth eigenfunction is the mean. It consists of two cosine and sine waves, for the real and imaginary parts respectively, indicating that two circles have been distorted originally. The division between the two cells is obvious by the vertical jump of the graphs of the eigenfuctions at $n = 100$. A reconstruction of the data with 14 eigenfunctions shows all but the smallest scale variation in the boundaries is captured.

We then considered synthetic data that mimic the gross features of the pinwheel regime. One cell is left with its center fixed, while the other cell exhibits rigid body rotation about the first. Eight overlaid snapshots of this regime are shown in Fig. 6. The variation of the outlines is constructed in exactly the same way as the previous example. The KL spectrum shows one mode with 99% of the energy in the first mode. This first mode, plotted in Fig. 7, represents the uniform shift of either cell center by a constant amount. Hence it is a step-like function, the left-half allowing for the shift of the center of the first cell, the right allowing

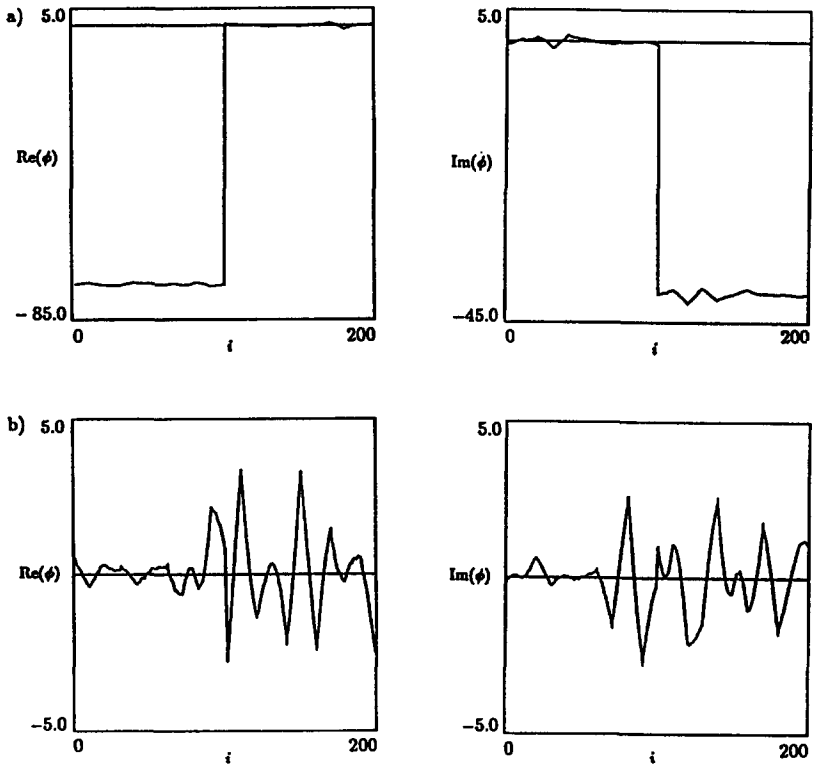

Fig. 7. (a) First eigenfunction, (b) Second eigenfunction, rotating data.

for the shift of the 2nd cell. The second mode is associated with reconstructing the shape of the two cells. The higher, less energetic eigenfunctions capture the variation in shape of each cell.

There is clearly a separation of length scales in this problem: the large scale rotational motion dominates the spectrum. The KL decomposition allows us to remove this motion from the data and decompose only the shapes of the cells. To do this, we simply subtracted the data reconstructed with the mean and first eigenfunction (i.e. the projection of the data onto the zeroth and first eigenfunction) from the original data, and performed the KL decomposition on the result. The KL spectrum of this data is broad (14 modes for 98% of the energy), indicating that the variance is now spread more evenly over a range of length scales. Subtracting the approximation to the data reconstructed from the mean and the first eigenfunction removes the rotation of the centers in this case, and is equivalent to moving into a co-rotating frame.

This result led us naturally to the idea that KL can be used to detect separation of length scales in such a pattern analysis problem, and also to isolate features of the motion that exist at widely separated length scales. In the same way that the mean can be subtracted out to give zero-mean data, large scale motion (like the rigid body rotation of the ratcheting regime) can be subtracted, leaving data that consists of the smaller-scale variation in the boundaries. In this way the resolution of the decomposition is limited only by the resolution of the data. Large scale motion need not dominate the analysis.

We explore these ideas in the section of KL analysis of the real flame data. In the next section we describe our technique for extracting the cell boundaries from the digitized video frames.

4. Processing video images of flames in motion

The video images described in Section 2 seem to indicate that the behavior of the flames is captured by changes of shape and position of their boundaries. As discussed in Section 3 we expect a KL analysis to yield useful information about the dynamics. Hence, we are confronted with the task of extracting and measuring the cell boundaries in a format suitable for a KL decomposition. In doing so, the dynamics of the flame cells are replaced with the dynamics of their boundaries. An appropriate representation of the boundaries for a KL analysis requires the following:

(1) Thin edges: Every cell boundary must be represented by a complex one-dimensional vector. In terms of the original image, this means that we need an edge detector to identify cell boundaries at single pixel locations. Otherwise, it is very difficult to correlate the evolution of a boundary as it evolves in time.

(2) Unsegmented edges: Every boundary vector should define a one-dimensional closed and continuous curve. Gaps between boundaries may result in edge linking problems and could eventually alter the dynamics.

(3) Noise free edges: The presence of noise in an image should not produce false edges. Similar shapes should be obtained within certain tolerances of the noise level.

(4) Constant resolution: Since a KL analysis is based on the correlation of points as they evolve in time, every cell boundary should have the same size. Variable size boundary vectors would certainly produce erroneous interpretations of their motion. Furthermore, every time snapshot should have a constant number of such vectors, even if the number of cells has changed.

(5) Cell identity: It is extremely important to generate a boundary-vector structure that maintains the identity of the cells as they move in time. Similarly, every point on a boundary vector must also be properly identified with points of the same boundary throughout a sequence of images. Hence, the ordering of the points within a vector is also important.

(6) Continuity: All of the above requirements apply to every snapshot in a sequence of video images. The algorithm should work well with as many images as possible, and should be able to extract all boundaries for all images. This is particularly useful and important when studying fast motion.

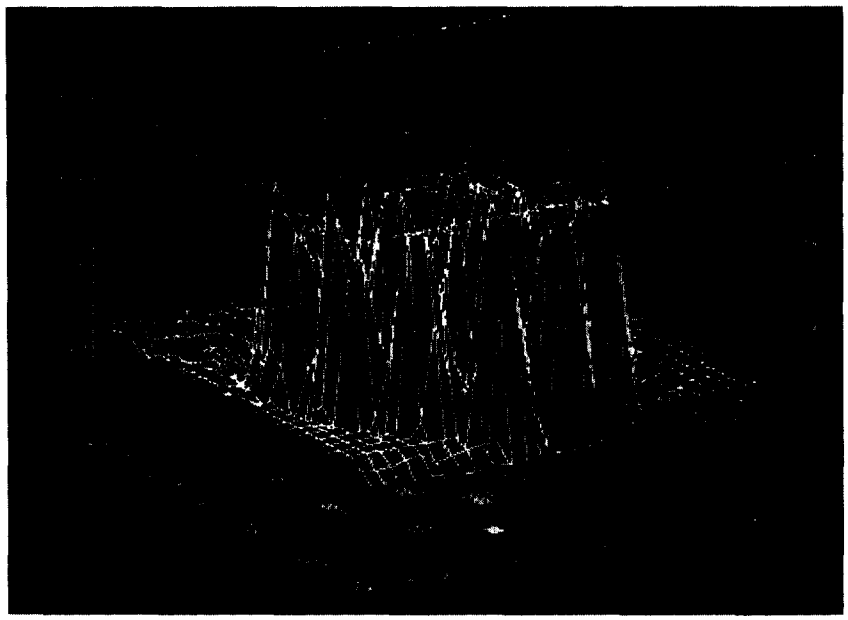

Fig. 8. A gray-scale image rendered as a surface.

A small time-resolution may significantly change the dynamics.

Most conventional image processing algorithms for edge detection, such as convolution operators, first and second derivative operators, morphologic operators, etc., do not satisfy the above requirements when applied to the flame images. Most of these algorithms only produce single pixel boundaries when applied to ideal images, i.e. images with perfect boundary constrasts. Originally, we applied a convolution operator and a morphologic edge detector (see [9,10]). The results were not satisfactory, because the fuzziness of the flame images makes it very difficult to obtain single pixel boundaries, and in most of the frames, there are always gaps in the boundaries. We successfully processed the data using a contouring method to detect a boundary and a marching algorithm to extract it as a complex one-dimensional vector.

The first step in preparing the video images is boundary detection. We wish to transform the image shown in Fig. 1 into a binary image. This is done by first considering the gray-scale image as a surface of the form: $z = I(j,k)$ where j,k are pixel coordinates with $0 \le j \le 319$, $0 \le k \le 239$, $0 \le z \le 255$. This surface is shown in Fig. 8. Note that each peak on the surface represents a flame cell. The boundaries of the cells are then obtained by contouring the surface at appropriate values, producing the binary image shown in Fig. 9. Observe that now all boundaries are one pixel wide and form closed, continuous curves. There are no gaps or phantom boundaries. An Image boundary is then defined as a set of level curves of the form $\partial I = \{(j,k) \mid I(j,k) = c$, where $c =$ constant$\}$. Ideally, we should be able to use the same value of c for every snapshot. Unfortunately the image intensity varies among the frames, and further study of the intensity distribution in the images is needed in order to adjust c to obtain good boundaries. Some regimes, like the rotating and ratcheting states, involve multiple rings of cells. We have found that the outer cells maintain an intensity distribution that is different from that of the inner cells; fortunately, they both are constant. This makes the contouring process easier. We inspected the intensity profiles of each ring and found two constants c_1 and c_2 that could produce optimal contour curves. Each ring is then contoured separately and the binary images are overlapped on top of each other, producing Fig. 9.

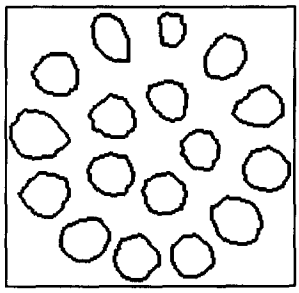

Fig. 9. Binary image after contouring.

The above process has to be repeated for every snapshot in a time sequence of video images. We have automated and implemented this routine in a Silicon Graphics workstation using the IDL (Interactive Data Language) software package.

The second step of the video processing involves the extraction of pixel coordinates from binary images in such a way that every cell boundary is identified and stored as a complex valued one-dimensional vector. A data structure is created to organize and store each complex vector. This is particularly useful when animating the motion of the boundaries. Pixel extraction is achieved using a "marching bug algorithm" described by Pratt [12].

The basic idea is illustrated in Fig. 10 which shows the boundary trace for a binary image consisting of three cells. The little numbers in the figure illustrate the path followed by the marching algorithm when extracting a cell. Each image is scanned from left-to-right and top-to-bottom to locate the first transition from a white background to a black pixel. The marching algorithm starts whenever such a transition is found. The basic principle is to let the bug move around in pixel space according to the following rules: if the bug makes a white-to-black pixel transition, it returns to its previous starting point, and makes a right turn. The bug makes a right turn whenever it

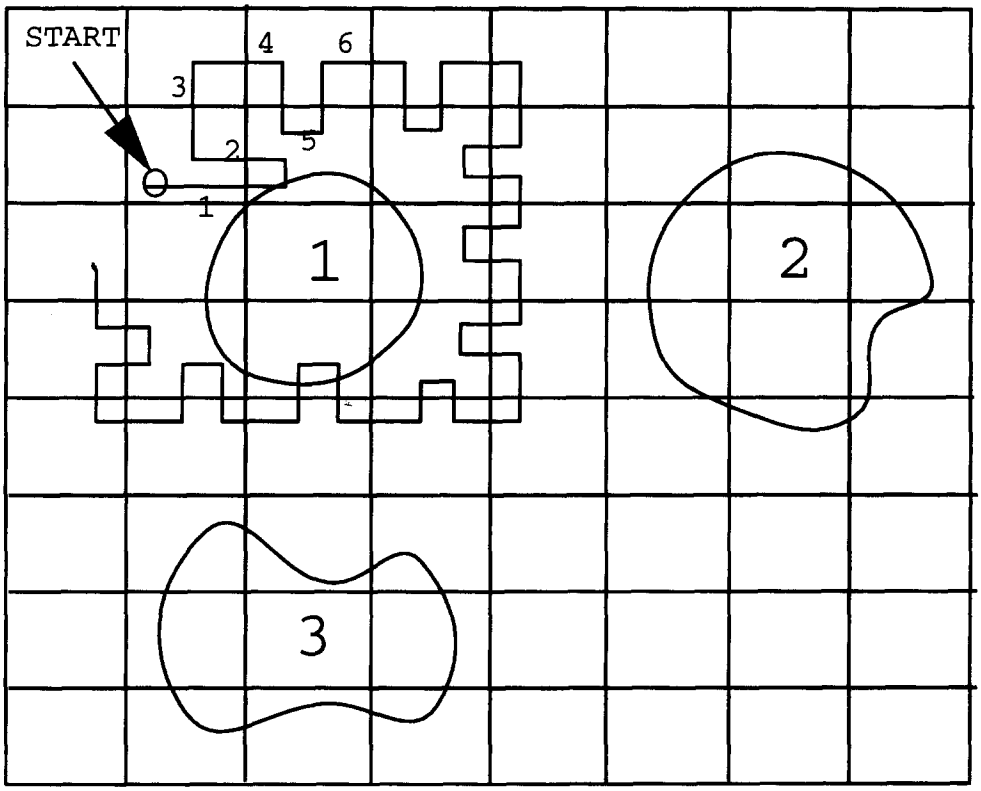

Fig. 10. Graphic example of the marching algorithm. Each square on the grid represents a pixel location.

makes a white-to-white transition. Every time a new pixel is found along the trace of the boundary, the algorithm records its position in a vector. Every cell boundary is described by a different vector. The procedure continues until the bug returns to the starting point. Upon completion of the boundary trace, the cell boundary is removed from the binary image by setting the intensity values of those pixel on the boundary to zero. We then continue scanning the binary image until another cell is found. This procedure is repeated until the last cell boundary is extracted. At the end, the marching algorithm produces a data structure in which the cell boundaries are organized in a series of lists according to their time evolution. Each list contains the cell boundaries found in some particular image.

We assume that a high temporal resolution of the images (i.e., a fast capturing rate) results in a smooth and continuous transition of the flame cells and their centers of mass. Visual observation of the images seems to confirm this hypothesis. Consequently, the identity of the cells can be preserved if they are sorted and stored according to the displacement of their centers of mass. However, one should be careful to ensure that a fast capturing rate is employed when examining regimes with fast motion scales. Otherwise, the centers of the cells can be erroneously correlated and can produce false results. The ordering of individual points on the boundaries, is determined automatically by the rules of the marching algorithm: a cell boundary is always traced clockwise starting with the leftmost higher point with respect to the image array.

Cell boundaries extracted by the marching algorithm are represented in the form of discrete one-dimensional vectors of variable size. Every entry in the vectors contains the (x, y)-coordinate of a point on the boundary. The size of each vector depends on the number of pixel that identifies a boundary. Small cells produce small vectors, while big cells result in long boundary vectors. Since the time evolution analysis of the flame boundaries is based on their space correlation, we must ensure that all vectors have equal size. We accomplish this by first interpolating a cubic B-spline through the boundary points, then tracing the interpolated curve with an equal number of points. Once the cell boundary is interpolated by a cubic B-spline $s(u_i)$, we can obtain a fixed number of points on it by tracing $s(u_i)$ with an equal number of parameter values. In this way, all boundaries are represented by equal size vectors and can be correlated without problems.

4.1. Computational details

The number of boundary points is limited by the spatial resolution of the video camera. Zooming into one cell and representing the data with too many boundary points implies having more than one boundary point for an original data pixel. Hence any subsequent KL procedure analyzes in parts the correlation due to the pixel structure of the video recording. Typically we used 30–50 boundary points per cell. Within that range our results did not depend on the exact number of points chosen.

The KL results reported below did not depend much on the number of snapshots taken. However, in cases where a slow rotation is present we have taken care to analyze a set of snapshots that represent full multiples of the slow period. Again, it did not matter how many periods are captured and analyzed.

Manual intervention in the boundary extraction process was needed in a few times to discard frames for which no contour value could be found that would successfully and automatically detect all edges. In the most noisy dynamical regime this happened in less than 5% of the snapshots. Once the cell boundaries were detected, the marching algorithm was always able to extract them and no further manual intervention was needed.

For a typical regime with 250 images and a spatial resolution of 320×240 pixels, the boundary extraction process usually took about 3 h. The KL decomposition of the same number of images was usually performed in about 10 min.

The frame rate employed to transfer the flame images from video tape into the computer is technology dependent. Currently we can use a maximum of 30 frames s^{-1} with limitations in the spatial resolution

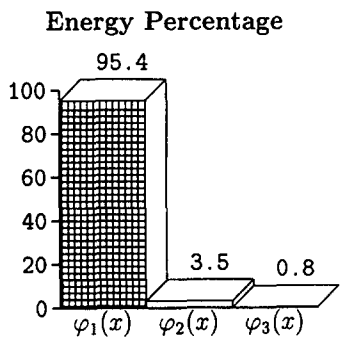

Fig. 11. Eigenvalue spectrum of a rotating state.

and the amount of frames that can be captured overall. An unproblematic rate is 15 frames s^{-1} which has been used in all computations except the fast rotating pinwheel regime. The frame rate is clearly dependent on the maximal velocities of the flame cells. We need to be able to correlate the position of a cell from one snapshot to the other. With 15 frames s^{-1} the counterclockwise rotating pinwheel regime showed spurious clockwise motion which went away when we increased the frame rate to 30 frames s^{-1}.

5. KL analysis of the flame data

5.1. Rotation

Using the technique described in Section 4 we processed 249 frames of the rotating regime and performed the KL decomposition on this data set. The eigenvalue spectrum showed that 99% of the variance is captured by the first three eigenfunctions, (see Fig. 11) and in fact, 95.4% of the variance is contained in the first mode alone. In Fig. 12 we plot the first three eigenfunctions, real and imaginary parts. Since the cells in the outer ring are ordered and stored first, the first 390 points (in every vector) represent the twelve cells in the outer ring (30 points per cell). The last 210 points represent the cells in the inner ring. The step-like shape of φ_1, shown in Fig. 12(a), represents a uniform shift of each cell center by a constant amount. There are seventeen steps; the first twelve account for each of the cells on the outer ring, and the remaining five for the inner ring. Since the inner ring remains steady throughout most of the sequence, the jumps on the last five steps are significantly smaller compared

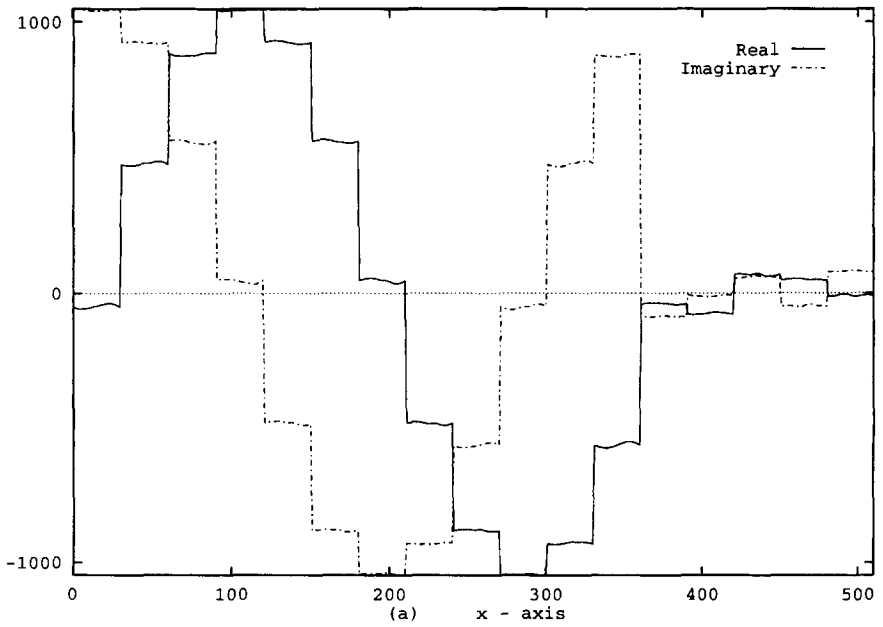

Fig. 12. The first three eigenfunctions, real and imaginary parts, obtained by the KL decomposition of a rotating state with alternating speeds: (a) first eigenfunction φ_1; (b) second eigenfunction, φ_2; (c) third eigenfunction, φ_3.

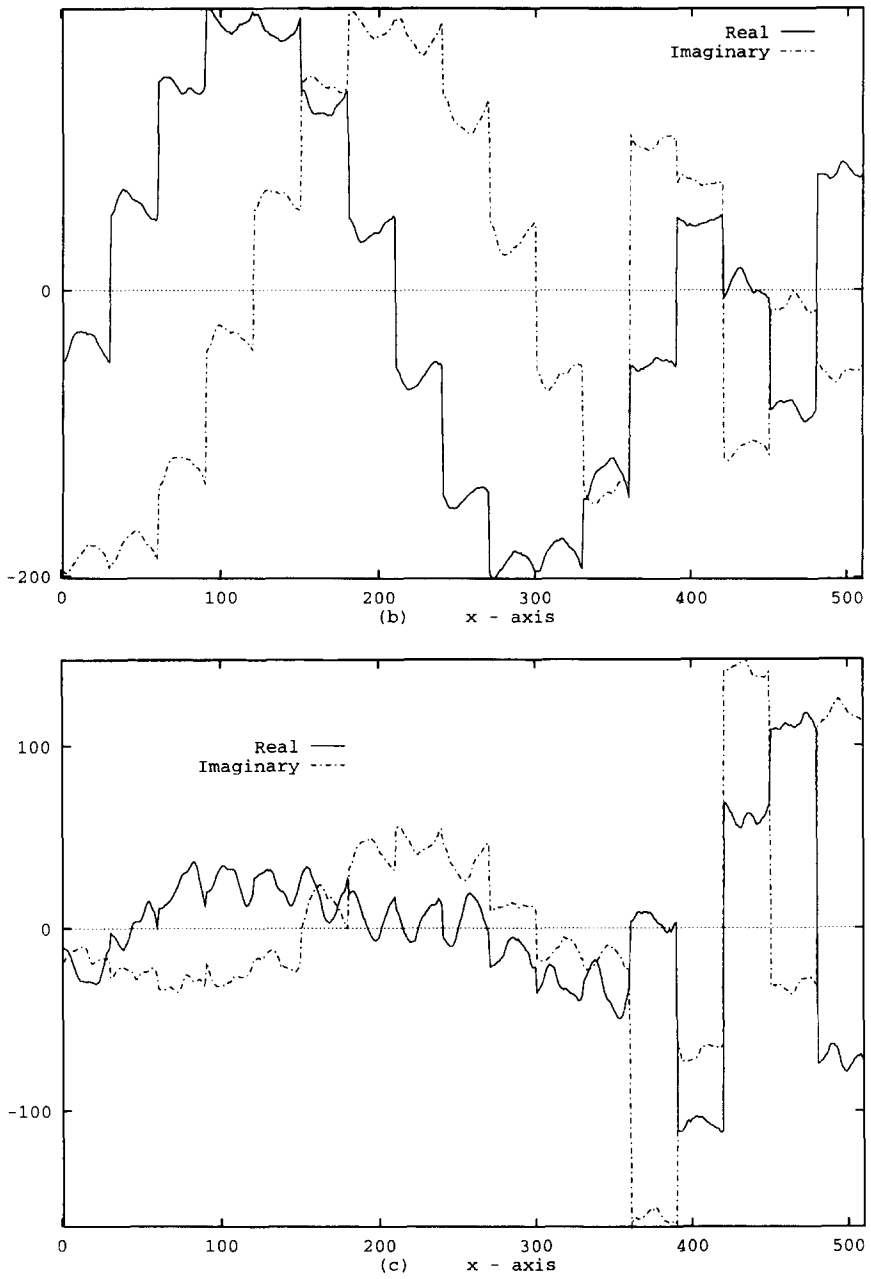

Fig. 12. (continued)

to the first twelve. In order to understand the contribution of the next two modes, we reconstructed the dynamics with one, two and three eigenfunctions. The reconstruction with one eigenfunction, φ_1, is a poor approximation. Indeed, it only captures a constant rotation of the centers of mass of each cell on the outer ring. When φ_1 and φ_2 are used in the reconstruction, the outer ring moves with alternating speeds and the shapes of the cells improve slightly. However, the inner ring remains fixed. The distorted sine and cosine waves observed in the jumps of φ_2 (see Fig. 12(b)) contain information about the speed of the outer ring and

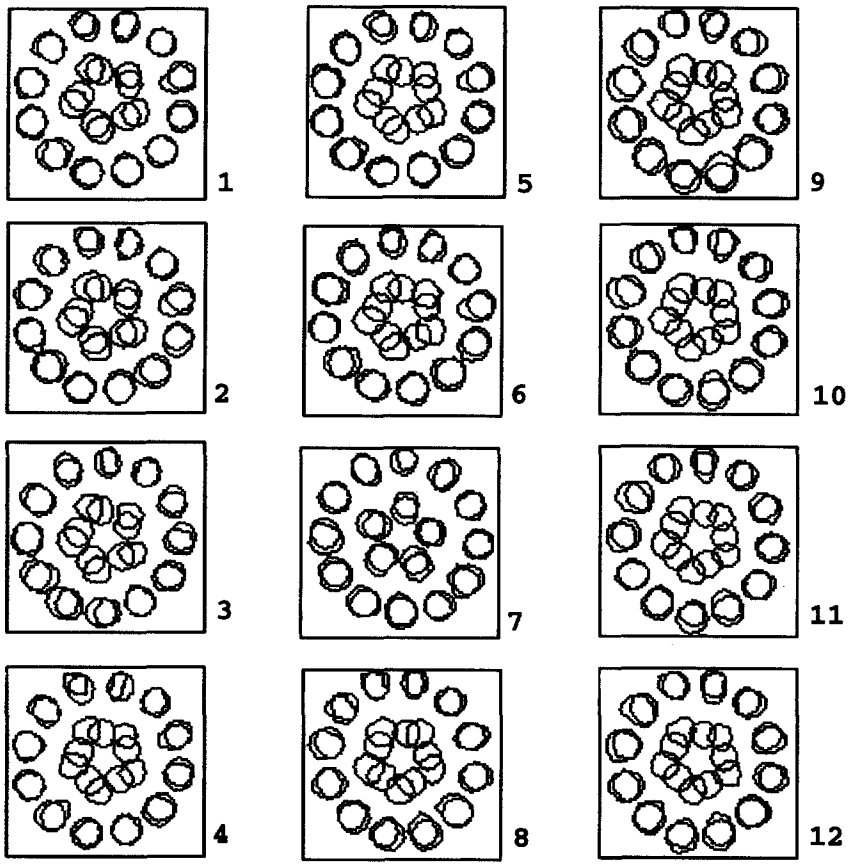

Fig. 13. Reconstruction of a rotating state. In red, the original data; in black, the reconstruction with two eigenfunctions. The inner ring fails to move.

some information about the shape and size of the cells. Fig. 13 shows in red the original boundary data and in black the reconstructed data with two eigenfuctions.

When the thrid eigenfunction, φ_3 is added to the reconstruction, the inner ring rotates (Fig. 14). It rotates at the beginning and near the end of the sequence as observed in the original data. Fig. 12(c) shows that the third eigenfunction is very small for the outer ring and is therefore, responsible for the motion of the inner ring.

Although we get the temporal dynamics right and the shape and size of the cells improve with a three mode reconstruction, there are still significant differences visible between the data and the reconstructed cells. To obtain further information, we decided to decompose (using the KL decomposition) the error in the approximation with three eigenfunctions. A very broad KL spectrum was obtained: 55 eigenfunctions capturing 95% of the energy with no dominant eigenfunctions. The consequences of this observation, and similar ones that occur in other regimes, are discussed in more detail in Section 5.4.

The precise times when the angular velocity of the outer ring alternates between a low and high value are difficult to obtain from visual inspection. However, the amplitude coefficients of the approximation can be very useful for this purpose because they are time dependent variables. In Fig. 15, we have plotted the real and imaginary part of the first two coefficients. The observed sine and cosine shapes represent the 360° rotating cycle of the outer ring. The little steps that perturb the otherwise perfect sine or

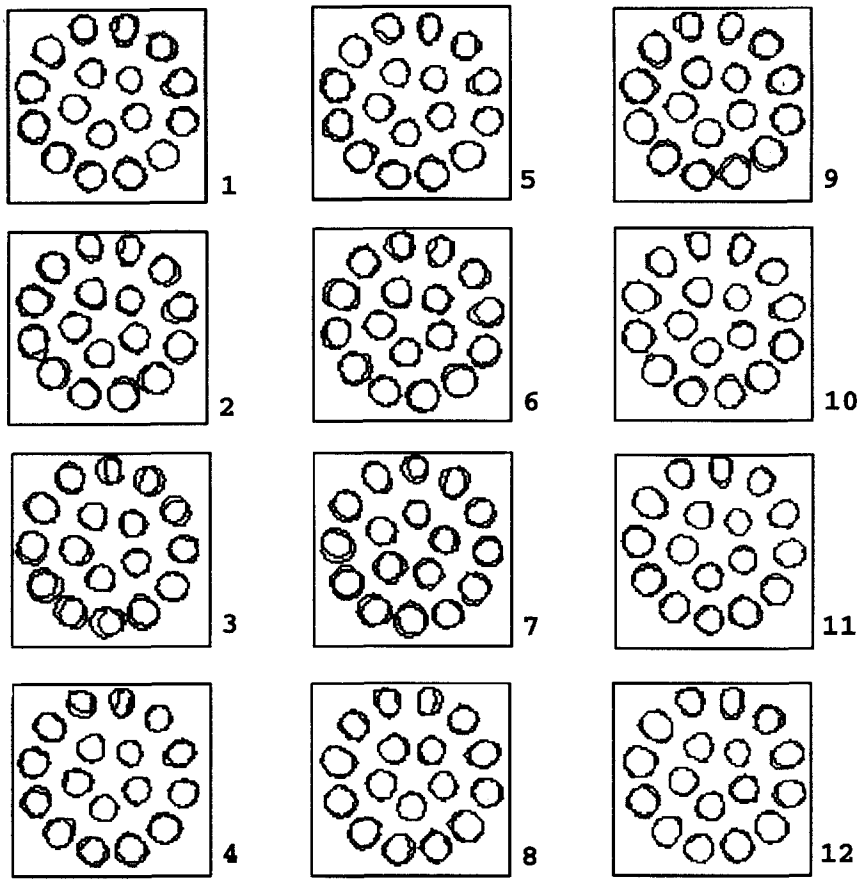

Fig. 14. Reconstruction of a rotating state. In red, the original data; in black, the reconstruction with three eigenfunctions. The reconstructed inner ring now follows the rotation in the data set.

cosine function indicate the times when the outer ring slows down. These steps appear periodically. The flatness of these steps shows that the outer ring stops momentarily. In fact, a closer look at the reconstruction and the original data indicates that the outer ring stops periodically, corresponding to a ratcheting type motion. Hence there are at least two frequencies of rotation present, as in a dynamical system on a torus. However, this analysis does not take the fast inner rotation into account that happens towards the end of the data set. Evidently the torus has an unstable manifold in the full space of the motion. Unfortunately our data set is much too small to analyze the instability and the subsequent return of the motion to the torus.

5.2. *Pinwheel*

Our boundary extraction algorithm has been applied to the pinwheel regime. The extracted cell boundaries are ordered based on the angular position of their centers of mass while preserving their identity during the rotation of the ring. Every cell boundary is interpolated to produce one-dimensional complex vectors with 50 points per vector, i.e. every boundary is represented by $50(x, y)$ points. We then apply the KL decomposition to these boundaries and obtain the eigenvalue spectrum of Fig. 16. It shows one dominant mode, φ_1, capturing most of the dynamics with 98.1% of the energy. The second mode, φ_2, still captures a significant amount of energy, 0.9%. The rest

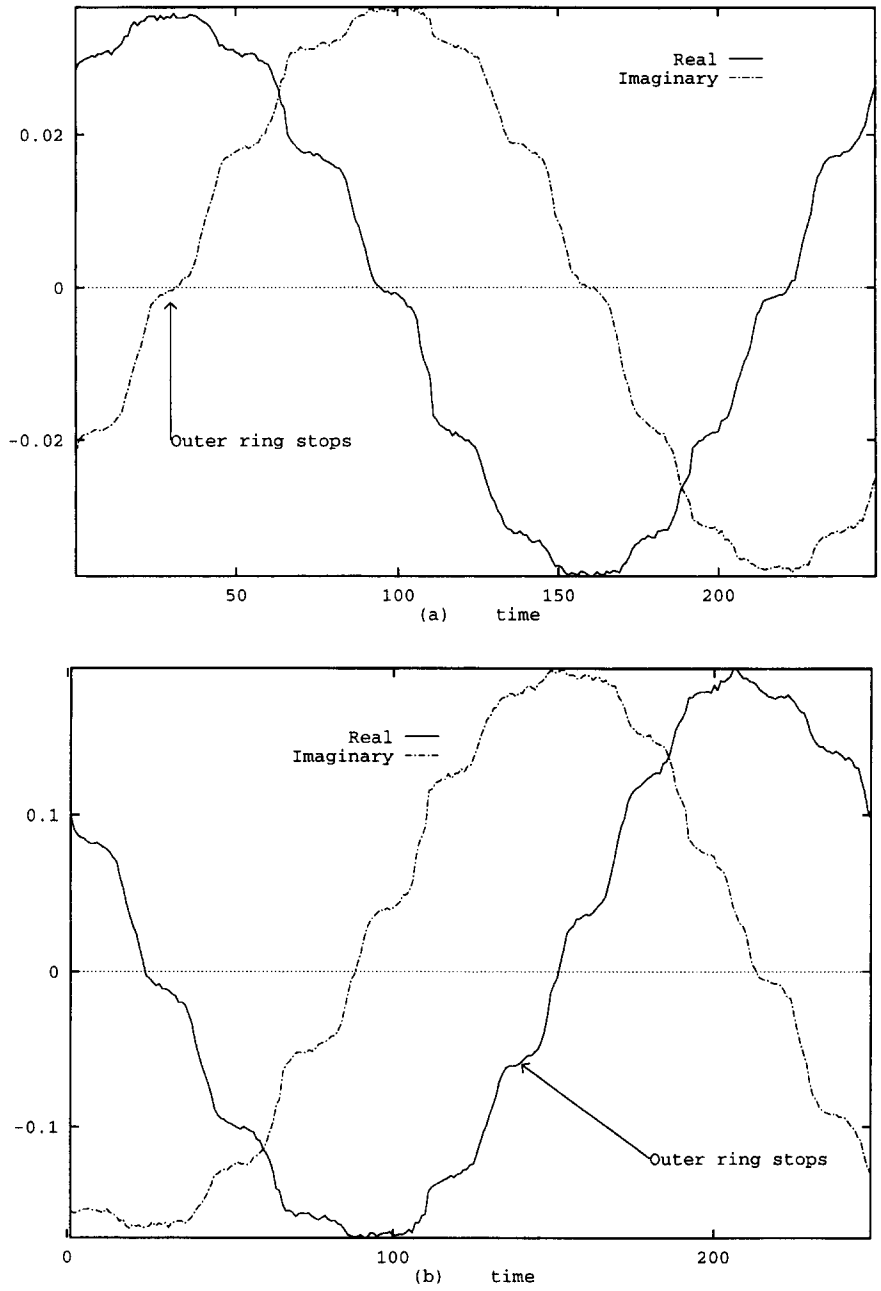

Fig. 15. The real and imaginary parts of the first two amplitude coefficients in a rotating state: (a) first coefficient, $a_1(t)$; (b) second coefficient, $a_2(t)$.

of the modes are much less energetic with a uniform distribution of energy.

We have plotted the real and imaginary parts of the first three modes in Fig. 17. The first six vectors ($0 \leq x \leq 300$) represent the cells in the ring, and the last vector ($301 \leq x \leq 350$) is associated with the central cell. The almost step-like shape of Fig. 17(a) suggests that φ_1 is associated with the rotation of the centers of

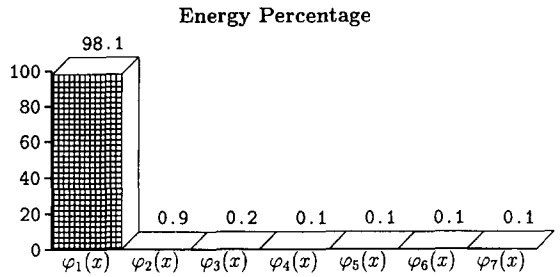

Fig. 16. The eigenvalue spectrum for a fast rotating ring of cellular flames. The first and most energetic mode, φ_1, captures most of the dynamics with 98.1% of the energy.

mass of the outer cells. Observe that $\varphi_1(x)$ is close to zero for $301 \leq x \leq 350$. This indicates that the first mode has no contribution to the dynamics of the central cell; it only reconstructs the motion of the ring. While small deviations from a step size function in φ_1 indicate the presence of almost circular outer cells, the major shape variations for the boundaries of the cells in the ring begins to appear in the second mode, φ_2, shown in Fig. 17(b). The contribution of φ_2 towards the dynamics of the central cell is also low. Fig. 17(c) shows the third and least energetic mode, φ_3. The motion of the central cell is now visible, although still small compared to the magnitude of the other cells. This mode contains more shape information for the cells in the ring. All other eigenfunctions have no distinguishable scale separations between the cells in the ring and the central cell. The broad spectrum with uniform energy distribution of the remaining eigenfunctions suggests that the remaining boundary motion may be turbulent (see below).

We reconstruct the dynamics by projecting the boundary vectors onto a finite number of eigenmodes, and obtain the following results. With one mode, only the cells in the ring move, the inner cell is always fixed (as expected) and the centers of mass in the approximation are slightly off. With two modes, the cells in the ring rectify their phase, and the reconstructed ring is able to follow closely the fast rotation of the original data. A small variation in the shape of the cells in the ring is added, the middle cell starts oscillating and the shape and size of all cells improves slightly. The periodicity of the first two amplitude coefficients, plotted in Fig. 18, suggests that the long-term behavior is captured by a limit cycle. Indeed, a limit cycle is visualized when the two first coefficients $a_1(t)$ and $a_2(t)$ are plotted against each other. The motion of the center cell (Fig. 18(c)) is represented by what seems to be a weakly chaotic time series that should be studied further on a much longer data set.

5.3. Ratcheting

We analyze a recorded sequence of 406 video images in which the ratcheting cycle repeats itself periodically, about 18 times, and the outer ring executes a rotation of approximately 500°. Using the procedure outlined in Section 4, the boundaries of the cells are obtained by contouring the outer and inner rings separately with two intensity values of 68 and 110, respectively. Each boundary cell is represented by 30 points. The thirteen cells in the outer ring are sorted sequentially based on the angular displacement of their centers of mass. They are also stored before the cells in the inner ring. In this way, each snapshot is represented by a one-dimensional vector with 600 points. The first 390 points define the outer ring (13 cell boundaries of 30 points each) and the remaining 210 points represent the inner ring and the central cell.

The KL decomposition is applied to the boundary vectors and produces the eigenvalue spectrum of Fig. 19. Remarkably, 99.7% of the energy is captured with only three eigenmodes. The first one, φ_1, dominates the dynamics with 96.3% of the energy. The second eigenmode, φ_1, contains 13.3%, and the third one, φ_3, only absorbs 0.1% of the energy. The real and imaginary parts of the first three eigenfunctions

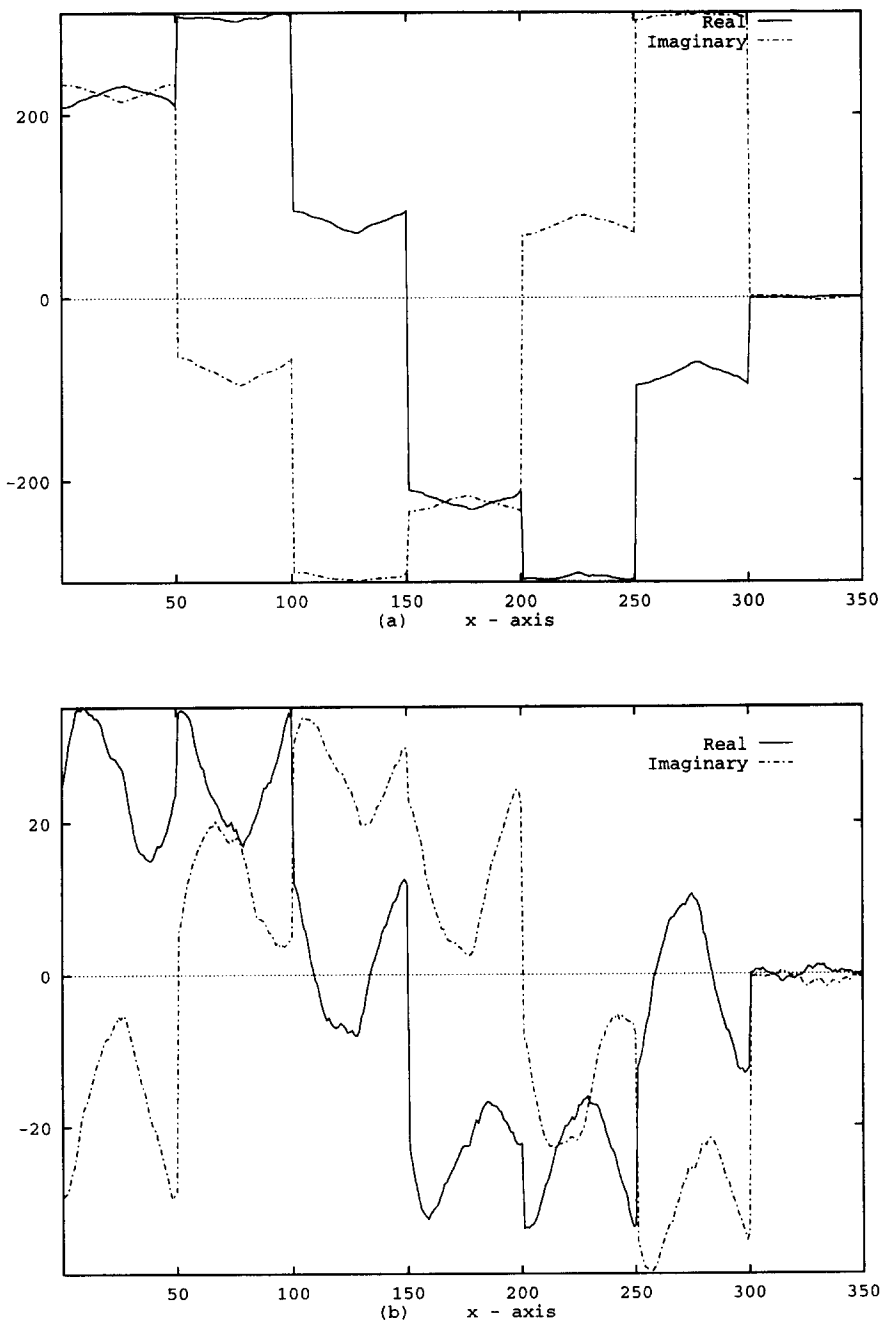

Fig. 17. The first three modes in the KL decomposition of a fast rotating ring of cells. Their real and imaginary parts are plotted in two separate columns: (a) First mode, φ_1; (b) second mode, φ_2; (c) third mode, φ_3.

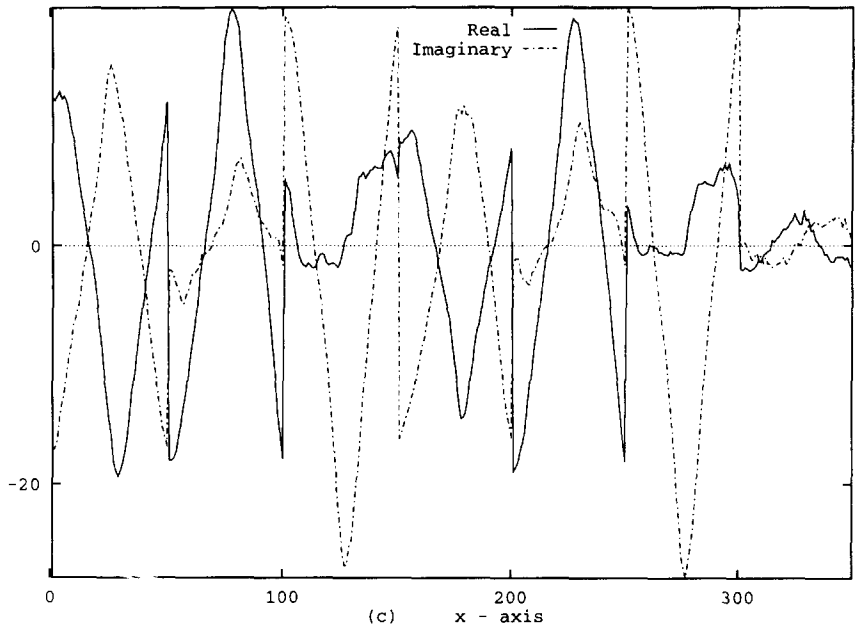

Fig. 17. (continued)

are depicted in Fig. 20. The first mode, $\varphi_1(x)$, represents a uniform shift of each cell center by a constant amount. It is zero for $391 \leq x \leq 600$, which corresponds to the boundaries of the cells in the inner ring. This indicates that only the centers of those cells in the outer ring are shifted. The sine and cosine waves found in the second mode, $\varphi_2(x)$, correct the phase of the centers and add shape information to the first eigenmode. Surprisingly, $\varphi_1(x)$ and $\varphi_2(x)$ are responsible only for the motion of the outer ring. The dynamics of the locking and unlocking of the two rings has no effect on the first two eigenfunctions. The third mode constains information on both the outer and inner ring. A small scale variation, observed for $0 \leq x \leq 390$, is associated with the spatial complexity of the boundaries of the cells in the outer ring. The larger scale variation, for $391 \leq x \leq 600$, captures the ratcheting motion (locking and unlocking) of the inner ring. In summary, the dominant dynamics of the two rings is uncoupled by the KL decomposition.

As expected the reconstruction with two modes gives a reasonably good agreement for the motion of the outer cells but fails to capture the ratcheting of the inner cells. Including the third mode we find an almost perfect agreement for the motion of the inner cells. The shape of the outer cells improves slightly but, in general, it changes very little. We have applied the KL decomposition onto the error generated in the approximation with the first three modes to obtain more shape information for the cells. A broad eigenvalue spectrum appears with 60 modes capturing only 95% of the remaining energy, with no dominant mode. We thus deduce that the spatial pattern of the shape of the cells is highly complex.

The almost periodic time series of the first two amplitude coefficients, $a_1(t)$ and $a_2(t)$, shown in Fig. 21, respectively, suggests a limit cycle. The small components of the first two eigenfunctions in the inner cells (see Fig. 20) indicate there is a small but non-zero effect of the ratcheting inner cells on the outer ring. This appears as small periodic steps along the slope of $a_1(t)$ and $a_2(t)$. The third coefficient $a_3(t)$, shown in Fig. 22, shows the 18 periodic ratcheting cycles observed in the data set much more clearly. The individual high peak found in the amplitude coefficient $a_3(t)$ at $t = 240$ corresponds to an external event in the recording of the data. The periodicity of the first three amplitude coefficients suggest that the long-term

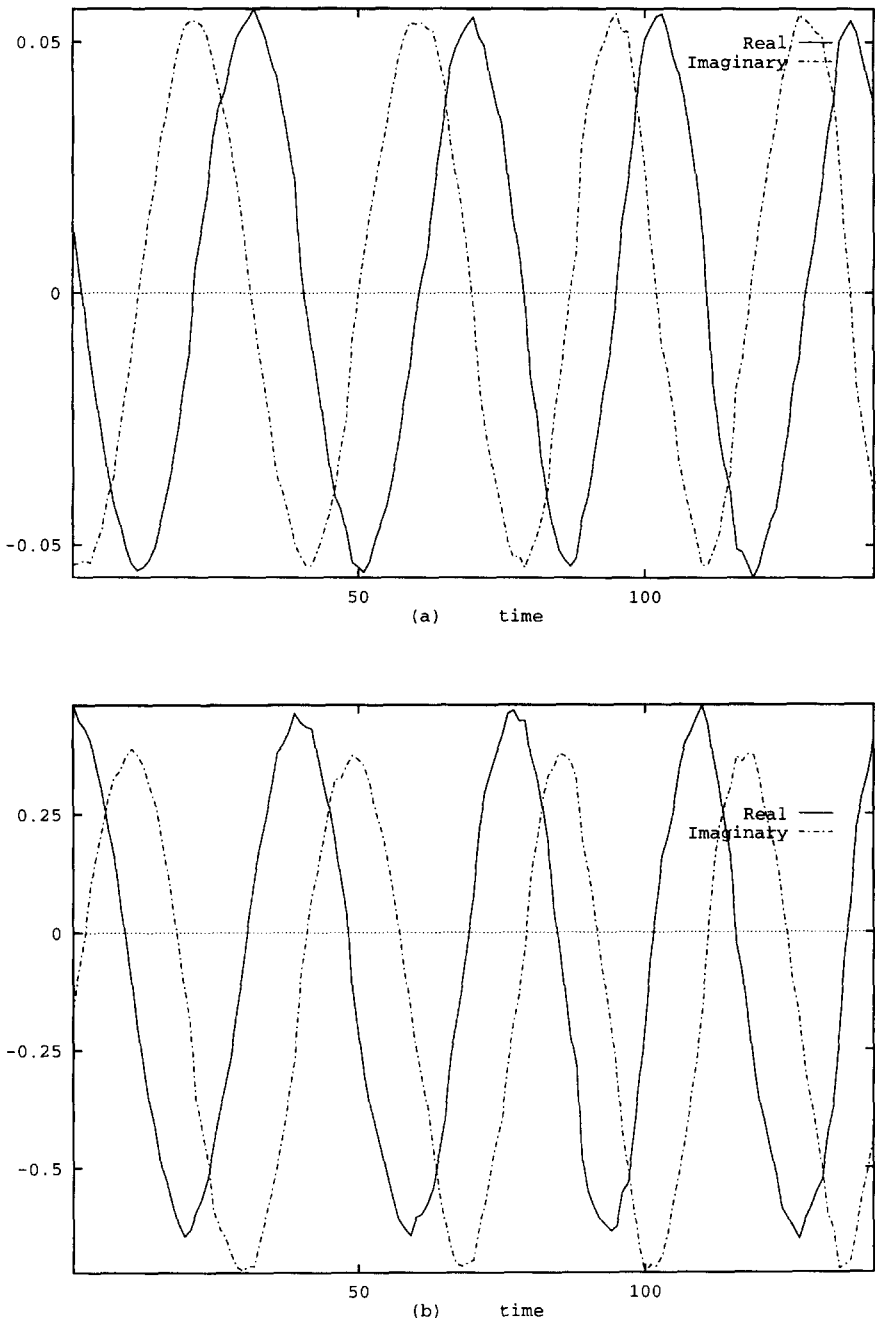

Fig. 18. The real and imaginary parts of the first three amplitude coefficients; (a) first coefficient, $a_1(t)$; (b) second coefficient, $a_2(t)$; (c) third coefficient, $a_3(t)$.

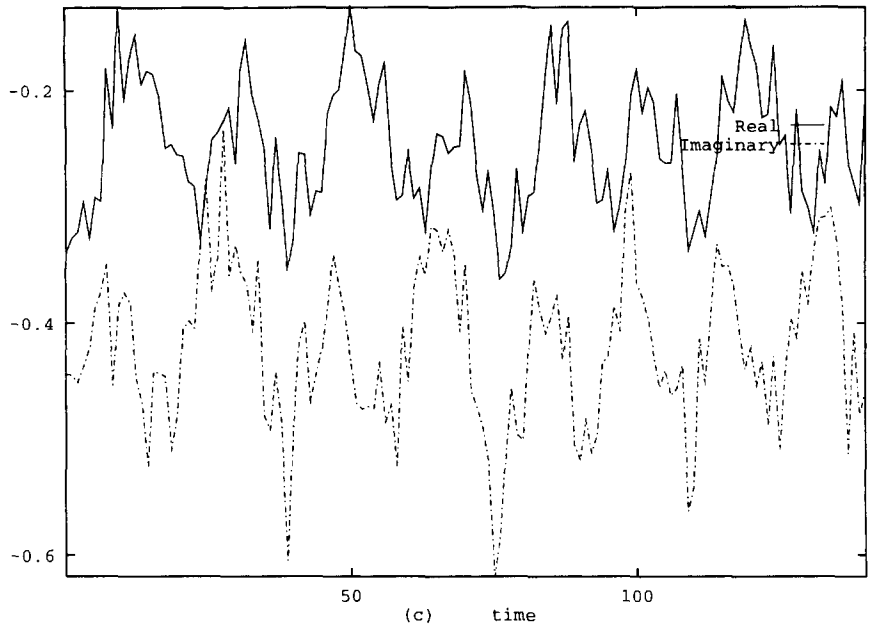

Fig. 18. (continued)

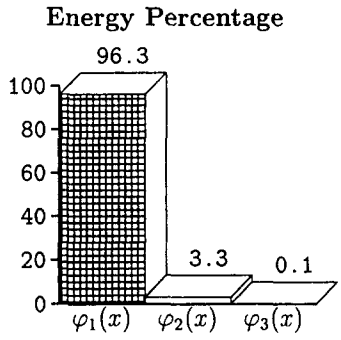

Fig. 19. Eigenvalue spectrum of a ratcheting state. Remarkably, 99.6% of the energy is captured by the first two corresponding eigenfunctions.

behavior of the ratcheting motion is described by a two-dimensional torus.

5.4. Intermittent states

Gorman et al. [14] report ordered patterns of states that initially seem to be stable. However, after a relatively long time they lose stability, and the pattern disintegrates or moves around irregularly until a new ordered pattern, or the old one, re-establishes itself. There is evidence that this intermittent behavior is related to homoclinic or heteroclinic cycles in the underlying phase space description of the system [14]. Since our data analysis requires a data vector of a fixed length, we cannot analyze the merging and disintegrating cells. However, we can try to analyze the patterns that appear as metastable states in such a regime. If these transitions are to be described by a homoclinic or heteroclinic cycle, we need first to establish the identity of the hyperbolic sets that are involved in those cycles. Fig. 23 shows a few snapshots of such an intermittent data set. In order to relate the states before and after the unstable phase, we apply the KL analysis to them separately and compare them. Both metastable states, before and after the unstable phase, have a substantial jittering dynamics and it is therefore, unclear whether any heteroclinic cycle should connect saddle fixed points or hyperbolic chaotic attractors. We find an unexpected and very interesting result: While the means of both data sets are almost identical (Fig. 24), the spectra of the jittering dynamics in both cases are very broad (see Fig. 25) and even the most energetic KL eigenfunctions are completely different from each other. This suggests that if there is a cycle governing

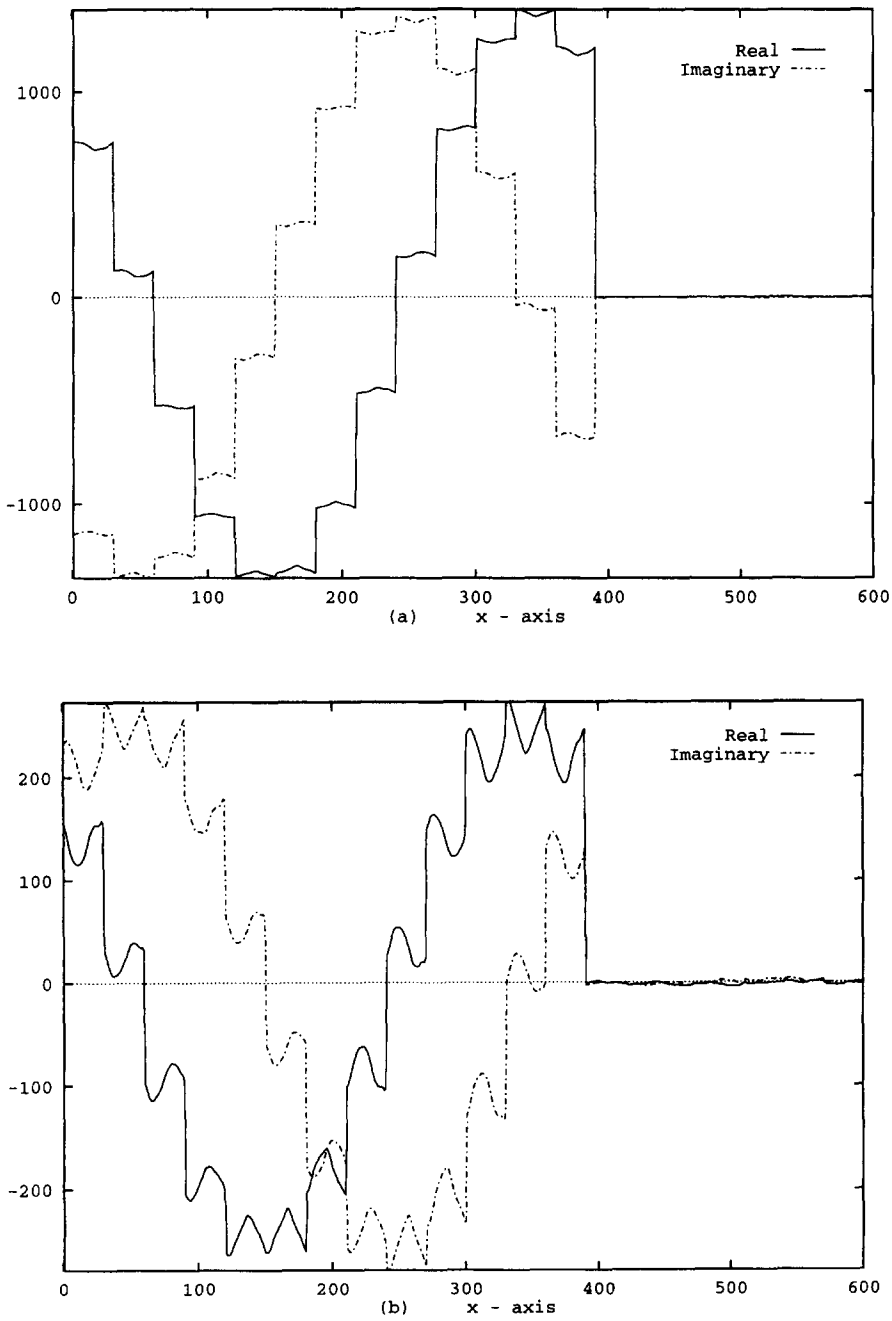

Fig. 20. The first three modes in a KL decomposition of a ratcheting state, their real and imaginary parts. Their domain separates two rings of boundary cells: the outer ring is found for $0 \leq x \leq 390$ and the inner ring for $391 \leq x \leq 600$.

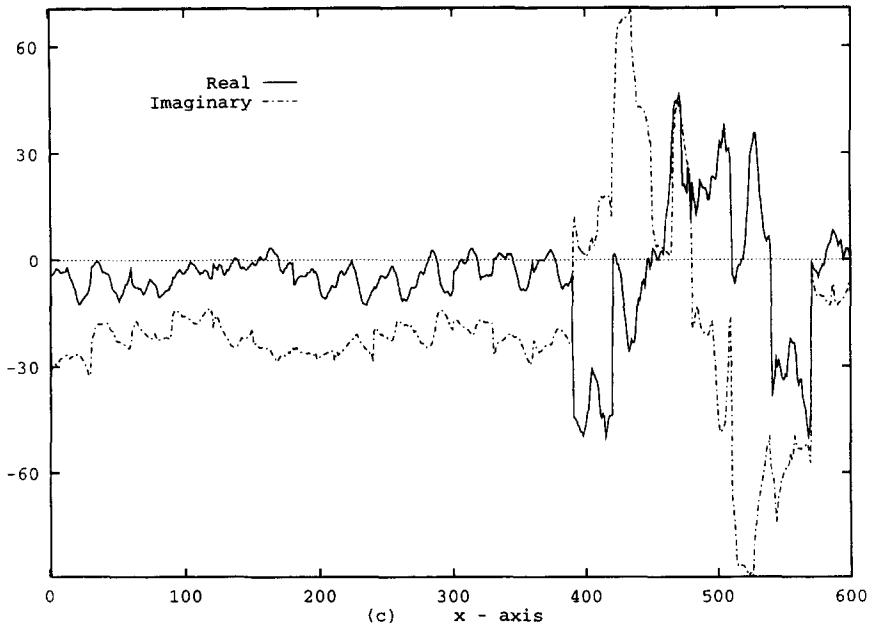

Fig. 20. (continued)

the intermittent behavior, it is homoclinic and connects a fixed point to itself. The remaining substantial jittering dynamics near that fixed point is better described as small scale, high frequency turbulence than as chaotic dynamics. As a typical example, we present eigenfunction # 5 of the first data set and the associated time series for the amplitude of the data projected onto this mode (Fig. 26).

6. Conclusion

This study is one of the few attempts to analyze spatio-temporally complex behavior of *experimental data* in terms of phase space structures. We have shown how to generate meaningful structures from rather noisy data on a videotape with limited resolution. The approach to extract the boundaries of the cellular flames by contouring a function of the pixel intensity, and the subsequent process that leads to well defined data vectors for each snapshot, can easily be applied to other similar experimental data.

The subsequent Karhunen–Loéve analysis of the boundary dynamics shows several interesting features:

- There is a very clear scale separation between the coherent structures that generate the low frequency, large wavelength dynamics and the broad spectrum of high frequency, small wavelength dynamics of the complicated background motion of the cells.
- In all of the regimes that were analyzed (the rigid rotating, the pinwheel and the ratcheting regime), we could reconstruct the large scale dynamics with three complex eigenfunctions with very good accuracy.
- In the rigid rotation and the ratcheting regime we find a doubly periodic phase space dynamics: a dominant limit cycle on top of which there is a faster, low amplitude modulation that generates ratcheting behavior. This suggests that these two regimes could be part of the same solution branch and may continuously deform into each other as the appropriate parameter is varied.
- The eigenfunction generating the ratcheting behavior has its dominant structure in the inner ring and is almost flat in the other ring. Hence the coupling between the rotating behavior of the outer

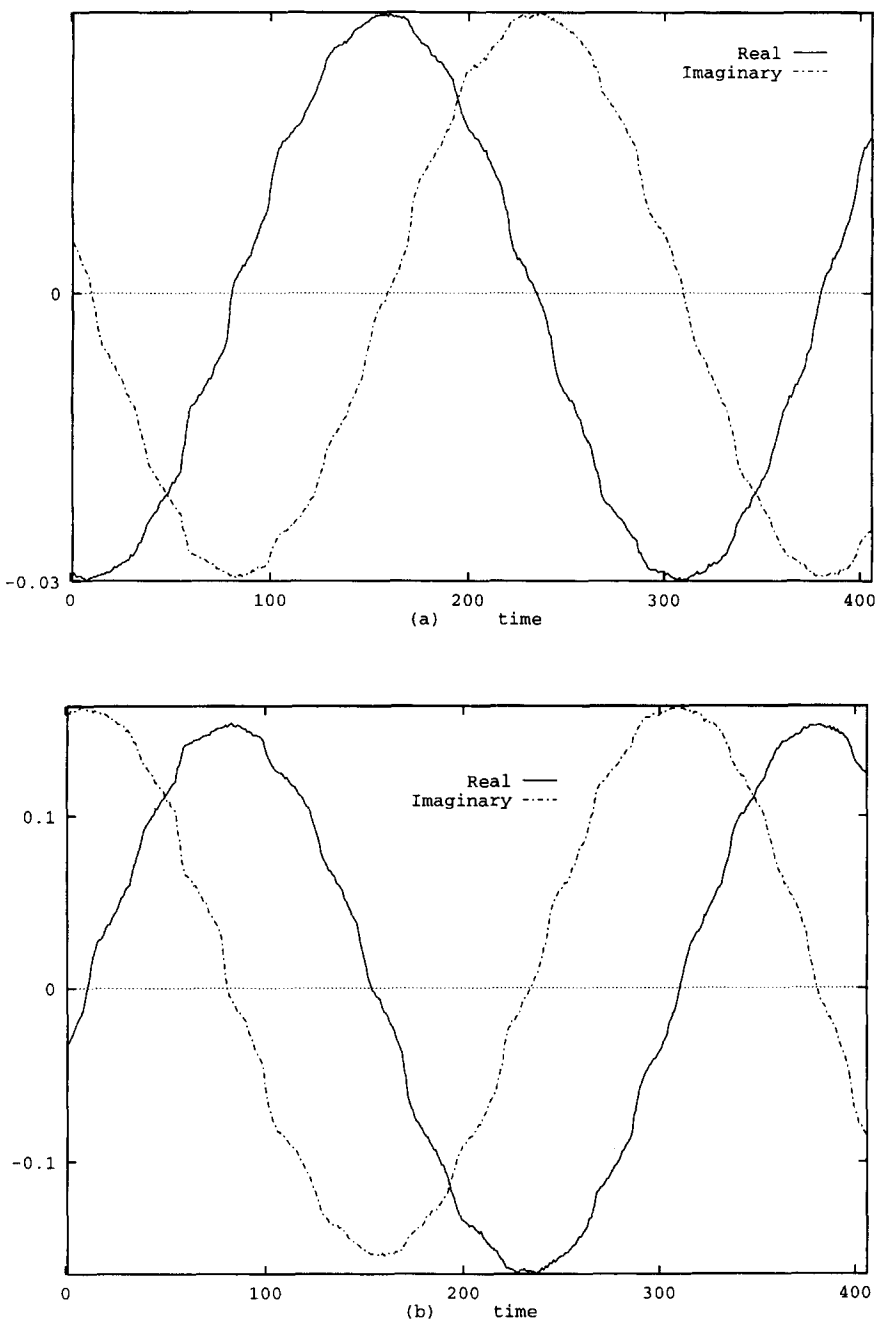

Fig. 21. The real and imaginary parts of the first two amplitude coefficients in a decomposition of a ratcheting state: (a) first coefficient $a_1(t)$; (b) second coefficient, $a_2(t)$.

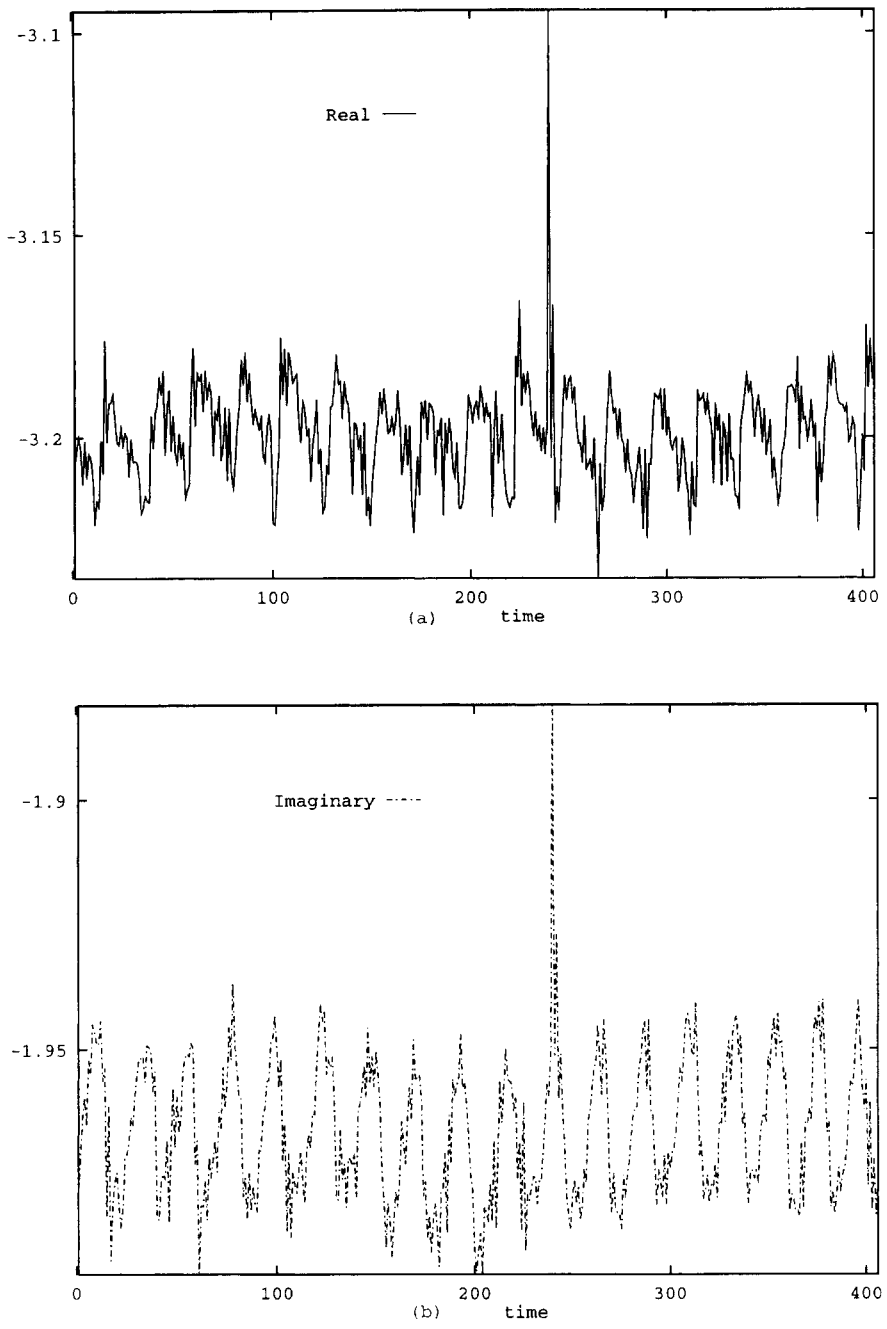

Fig. 22. The real and imaginary parts of the third amplitude coefficient, $a_3(t)$, in a decomposition of a ratcheting state: (c) the real part; (d) the imaginary part.

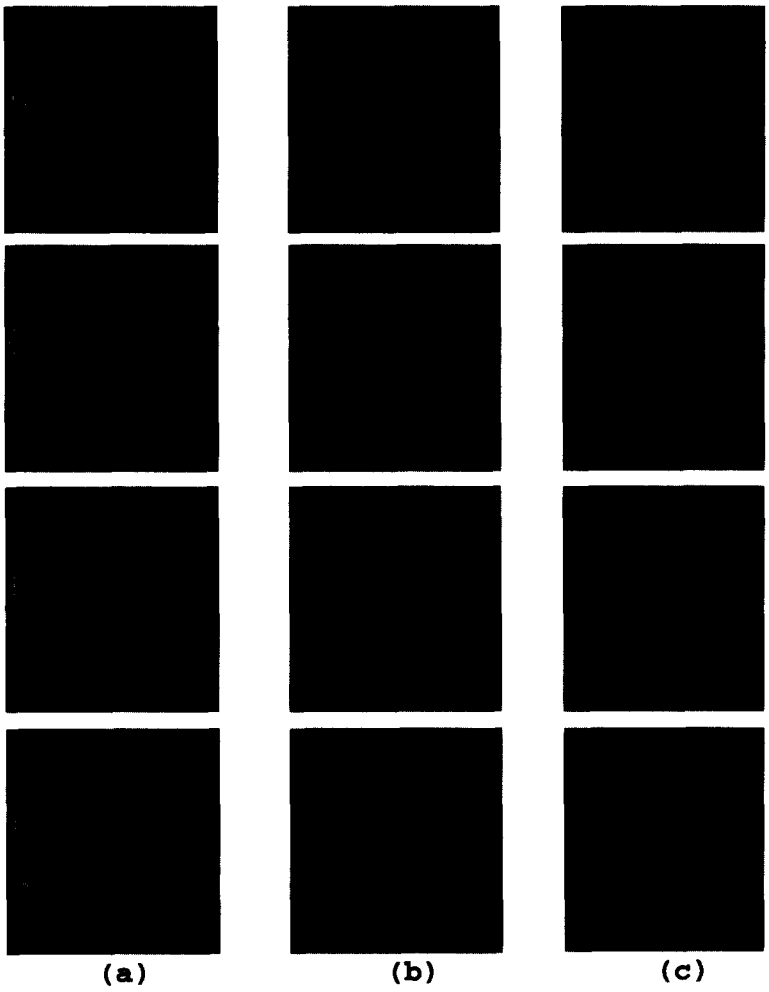

Fig. 23. Two ordered states in an intermittent regime: (a) The first pattern appears for 15 s; (b) a disorganized spatio-temporal sequence follows; (c) another pattern appears for 6 s.

ring and the periodic ratcheting inner ring is very weak.

- The pinwheel dynamics is characterized by a limit cycle describing the fast rotating structure and a possibly chaotic time series for the motion of the central cell.

These results put the dynamics of the cellular flames into the category of turbulent flows very much like the two-dimensional Navier–Stokes equation [2]. Typically, in those kinds of flows there are large scale coherent structures dominating the low frequency motion and a large number of high frequency, short wavelength modes that make up the stochastic, background dynamics. As a result, one might think about a pattern forming model of a reaction-diffusion type with diffusive length scale on the order of the large scale motion. This would not take into account the turbulent background which could then be modeled by a stochastic noise term.

To understand more about the background turbulence we are planning to take a much longer time series of one of these rotating regimes and, after elimination of the large scale motion, statistically analyze the remaining turbulent data set. In this way, we hope to extend the analogy between fluid turbulence and flame turbulence further with quantitative results.

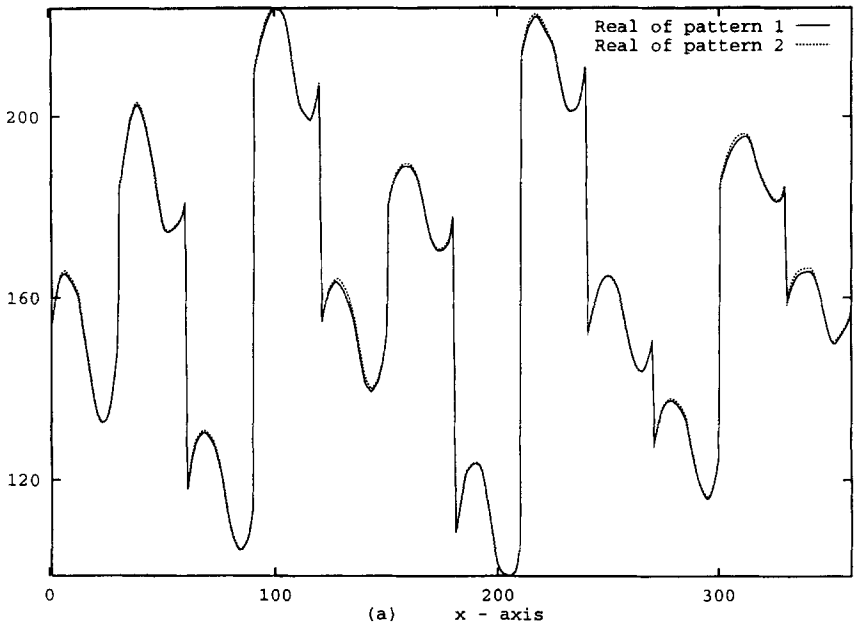

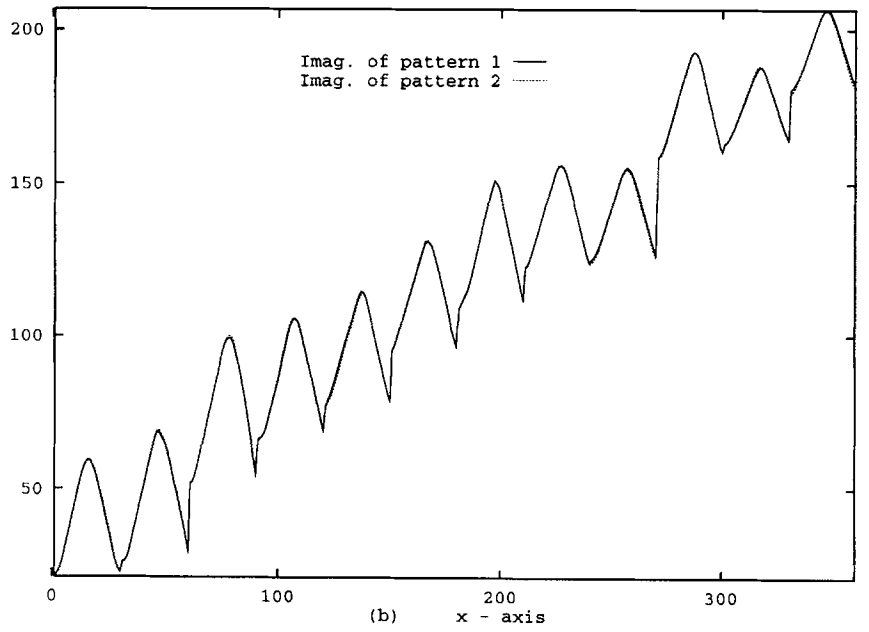

Fig. 24. The means of the two ordered patterns of Fig. 23.

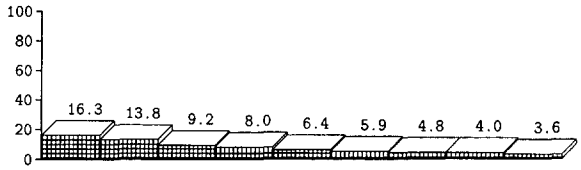

Fig. 25. Energy spectrum for the KL decomposition of an intermittent state.

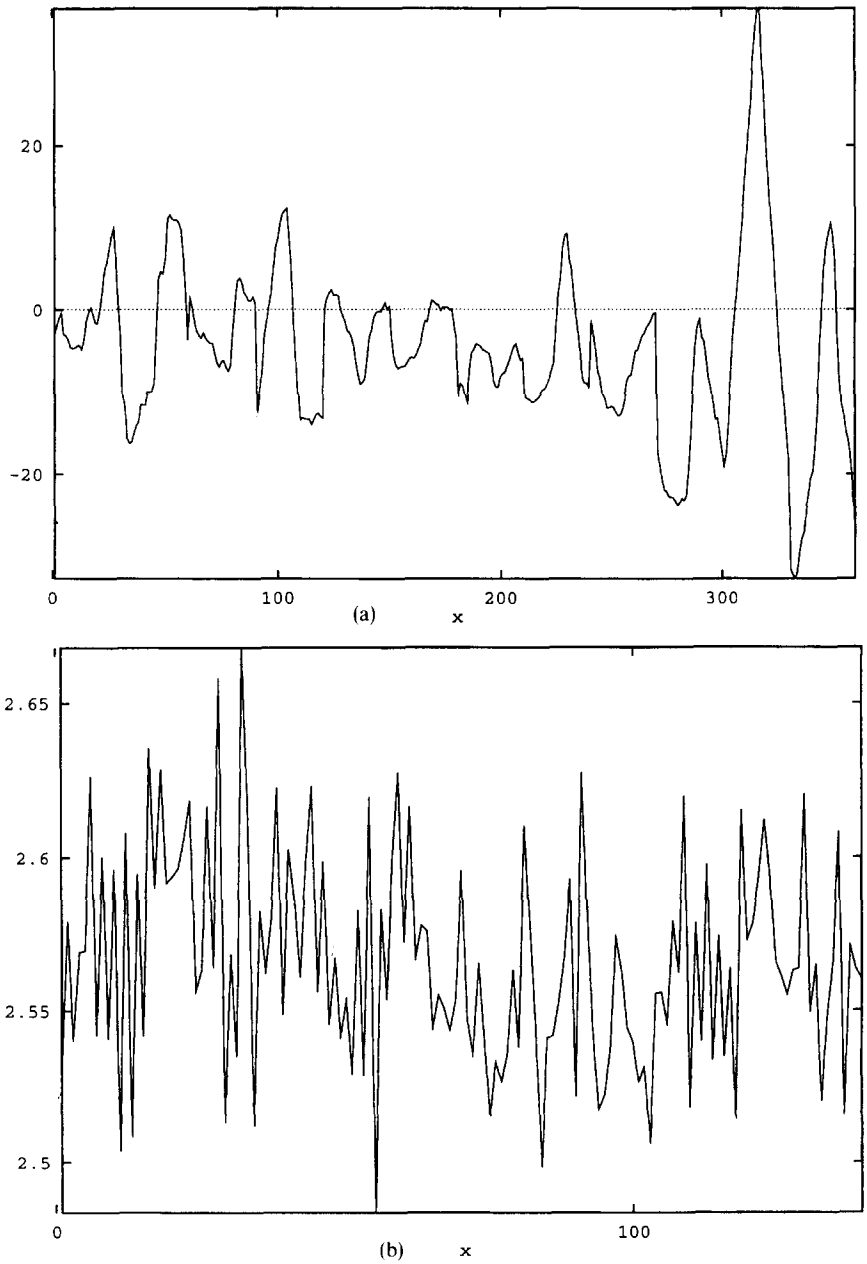

Fig. 26. Real part of eigenfuction # 5 and its time dependent amplitude.

Acknowledgements

We would like to thank Mike Gorman for providing us with the video data of his experiments. Support from NSF under grants DMS 9017174 and DMS 9101964 and from the Department of Energy under the grant DE-FG03-94ER25213 is gratefully acknowledged.

References

[1] D. Armbruster, R. Heiland and E. Kostelich, KLTOOL: A tool to analyze spatio-temporal complexity, Chaos 4 (2) (1994) 421–424.

[2] D. Armbruster, R. Heiland, E. Kostelich and B. Nicolaenko, Phase-space analysis of bursting behavior in Kolmogorov flow, Physica D 58 (1992) 392.

[3] N. Aubry, P. Holmes, J.L. Lumely and E. Stone, The dynamics of coherent structures in the wall region of a turbulent boundary layer, J. Fluid Mech. 192 (1988) 115.

[4] A. Bayliss and B.J. Matkowsky, Nonlinear dynamics of cellular flames, SIAM J. Appl. Math. 52(2) (1992) 396.

[5] G. Berkooz, P. Holmes and J.L. Lumley, The proper orthogonal decomposition in the analysis of turbulent flow, Ann. Rev. Fluid Mech. 25(75) (1993) 115.

[6] M. el-Hamdi, M. Gorman and K.A. Robbins, Deterministic Chaos in Laminar premixed flames: Experimental classification of chaotic dynamics, Combustion Sci. Technol., to appear.

[7] M. Gorman, M. El-Hamdi and K.A. Robbins, Spatio-temporal chaotic dynamics of pre-mixed flames, in: Proc. of the First Experimental Chaos Conf., eds. S. Vohra, M. Spano, M. Schlesinger, L. Pecora and W. Ditto (World Scientific, Singapore, 1992) pp. 403.

[8] M. Gorman, M. El-Hamdi and K.A. Robbins, Ratcheting motion of an ordered state of cellular flames, Combustion Sci. Technol., submitted.

[9] A. Huertas and G. Medioni. Detection of intensity changes with subpixel accuracy using Laplacian–gaussian masks, IEEE Trans. Pattern Anal. Mach. Intell. 8(5) (1986) 651.

[10] J. Lee, R. Haralick and L. Shapiro, Morphologic edge detection, IEEE Robotics and Automation 3(2) (1987) 142.

[11] J.L. Lumely, The structure of inhomogeneous turbulent flows, in: Atmospheric Turbulence and Radio Wave Propagation, eds. A.M. Yaglom and V.I. Tatarski (Nauka, Moscow, 1967) pp. 166–178.

[12] K.W. Pratt, Digital Image Processing, 2nd. Ed. (Wiley, New York, 1991) pp. 215–223.

[13] E. Stone, D. Armbruster and R. Heiland, Towards Analyzing the Dynamics of Flames, Fields Institute Communications 5 (1996) 1–17.

[14] E. Stone, M. Gorman, M. El-Hamdi and K. Robbins, Identification of intermittent ordered patterns as heteroclinic connections, Phys. Rev. Lett. 76(12) (1996) 2061–2064.

[15] L. Sirovich, Turbulence and the dynamics of coherent structures Parts I–III, Quart. Appl. Math. XLV 3 (1987) 561.